JGR Solid Earth

RESEARCH ARTICLE
10.1029/2018JB016993

Discriminating Between Causes of D″ Anisotropy Using Reflections and Splitting Measurements for a Single Path

Angelo Pisconti[1], Christine Thomas[1], and James Wookey[2]

[1]Institut für Geophysik, Westfälische Wilhelms Universität Münster, Münster, Germany, [2]School of Earth Sciences, University of Bristol, Bristol, UK

Key Points:
- Seismic anisotropy in D″ beneath the Atlantic is detected by using reflections and splitting of seismic waves
- Modeling of seismic anisotropy shows that mineralogy and deformation can be constrained if both methods are used along a seismic path
- Our observations are compatible with aligned postperovskite and a SW-NE deformation direction in the lowermost mantle beneath the Atlantic

Supporting Information:
- Supporting Information S1

Correspondence to:
A. Pisconti,
pisconti@uni-muenster.de

Citation:
Pisconti, A., Thomas, C., & Wookey, J. (2019). Discriminating between causes of D″ anisotropy using reflections and splitting measurements for a single path. *Journal of Geophysical Research: Solid Earth*, *124*. https://doi.org/10.1029/2018JB016993

Received 7 NOV 2018
Accepted 18 APR 2019
Accepted article online 26 APR 2019

Abstract Knowledge of deep mantle deformation is based on seismic anisotropy: the variation of seismic wave speed and polarization with direction. Measuring this directional dependency requires azimuthal seismic coverage at D″ depth—the bottom few hundred kilometers of the mantle—which is often a limit in retrieving the style of anisotropy. Shear wave splitting is the standard technique for probing mantle anisotropy, and recently, reflections from the D″ region have been used to infer azimuthal anisotropy. Here we combine observations and modeling of D″ reflections with shear wave splitting along a given raypath direction in order to constrain mineralogy and dynamics of the lower mantle. From our modeling, a clear distinction between different anisotropic media is possible by using both types of observations together but only one directional path. We focus on the lowermost mantle beneath the central Atlantic Ocean by using South-Central American earthquakes recorded in Morocco. We find complex azimuthal and distance variation for both polarities of D″ reflections and shear wave splitting parameters, which rules out a simple style of anisotropy—such as vertical transverse isotropy—for the region. Our preferred model consists of a phase transition from a randomly oriented bridgmanite to lattice-preferred orientation fabric in postperovskite, developed in a tilted plane sheared along a roughly SW-NE deformation direction.

1. Introduction

The *D*″ region (Bullen, 1949) is the deepest part of the Earth's mantle. Its role is fundamental for the dynamics of our planet, since it marks a thermochemical boundary layer (e.g., Lay, 2015) between the overlying convecting rocky mantle and the underlying convecting outer iron core. The D″ region encompasses seismic structures on different length scales, marking its complexity in terms of thermochemical heterogeneities (e.g., Garnero, 2000; Lay et al., 2004; Lay & Garnero, 2004; van der Hilst et al., 2007). It also causes scattering of seismic energy (e.g., Bataille et al., 1990; Brana & Helffrich, 2004; Mancinelli et al., 2016; Thomas et al., 1999; Vidale & Hedlin, 1998) and displays anisotropy (e.g., see Nowacki et al., 2011; Romanowicz & Wenk, 2017, for reviews). A phase transition from a magnesium-silicate bridgmanite to postperovskite (ppv) structure (Murakami et al., 2004; Oganov & Ono, 2004) has opened the possibility to explain some of these seismic features and reflections from the D″ discontinuity (Hirose, 2007; Lay & Garnero, 2007; Thomas et al., 2011; Wookey, Stackhouse, et al., 2005); however, not all deep mantle observations are easily reconciled with the ppv phase transition (Cobden et al., 2015).

Global tomography (e.g., Grand, 2002; Kárason & van der Hilst, 2001; Zhao, 2004) images long-wavelength structures at D″ depths, showing fast and slow regions often associated with subducted slabs and source regions of uprising, less dense material, respectively. These structures are likely the current snapshot of whole-mantle convection (e.g., Grand et al., 1997; van der Hilst et al., 1997), which in turn would induce deformation most likely acting on the upper and lower boundary layers (Kendall, 2000; Montagner, 1998) of the mantle, that is, lithosphere and D″.

Perhaps the most prominent evidence of mantle deformation is the presence of seismic anisotropy, which is the direction-dependent velocity and polarization of seismic waves. Anisotropy has been probed in the mantle in different geodynamic contexts (e.g., Maupin & Park, 2015), and by using seismic anisotropy, one can potentially infer information on deep mantle dynamics (Nowacki et al., 2011; Romanowicz &

Wenk, 2017; Walker et al., 2011). Global mantle anisotropic models (e.g., Panning & Romanowicz, 2006) help to distinguish different regions of anisotropy; however, while these models provide a broad picture of the anisotropy in the deep Earth, detailed information is necessary to further infer the dynamics and mineralogy of such a complex region.

Detailed studies using shear wave splitting report anisotropy in D″, for example, beneath Siberia (e.g., Thomas & Kendall, 2002; Wookey & Kendall, 2008), the Caribbean (e.g., Garnero, Maupin, et al., 2004; Maupin et al., 2005; Nowacki et al., 2010; Rokosky et al., 2006), the Indian Ocean (Ritsema, 2000), the Western United States (Nowacki et al., 2010), and the eastern and western Pacific (e.g., Long, 2009; Wookey, Kendall, et al., 2005). Strong changes in the style of anisotropy have been found at short scales across the border of the large low-velocity regions beneath Africa (e.g., Cottaar & Romanowicz, 2013; Ford et al., 2015; Lynner & Long, 2012, 2014a; Wang & Wen, 2007), the Pacific (Ford et al., 2006; Pulliam & Sen, 1998; Russell et al., 1998, 1999), and the Perm Anomaly beneath Eurasia (Long & Lynner, 2015), while inside the large low-velocity regions anisotropy seems to be smoother with vertically polarized shear waves faster than horizontally polarized shear waves (Romanowicz & Wenk, 2017).

A preferred method to study D″ anisotropy is the use of splitting measurements for waves traversing the D″ region (see, e.g., Kendall & Silver, 1998; Nowacki et al., 2011; Romanowicz & Wenk, 2017, for reviews). Recently, the *S-ScS* splitting method (Wookey, Kendall, et al., 2005) and differential splitting of *SKS* and *SKKS* (Lynner & Long, 2012) have been used to access different areas and to test variations in anisotropy across small scales. A different method involves using triplications of *S* waves due to the D″ discontinuity that were used to constrain the depth of the shear waves splitting onset and put constraints on the style of anisotropy measured by the splitting (Matzel et al., 1996).

Another approach to test deformation is the use of polarities of waves reflecting from a discontinuity (Saki et al., 2018; Thomas et al., 2011). Looking at azimuthal variation of the waveform polarities of the reflected *P* and *S* waves, azimuthal anisotropy can be observed and possible minerals and deformation styles can be tested. For this approach to be used on D″, the *P* and *S* wave reflections from the top of D″ must be visible in the seismic data. Those seismic reflections (called *PdP* and *SdS*) have been observed in many regions (see, Cobden et al., 2015; Lay, 2015; Wysession et al., 1998, for reviews), and reflections from the lowermost mantle have been interpreted as due to subducted slabs near the core-mantle boundary (CMB; e.g., Kendall, 2000; Thomas et al., 2004) also in combination with the ppv phase transition (e.g., Chaloner et al., 2009; Hernlund et al., 2005; Hutko et al., 2006; van der Hilst et al., 2007).

Estimation of velocity jumps across the D″ discontinuity, based on reflection amplitudes, can be used to infer mineralogy and chemistry changes responsible for the reflection pattern (Cobden & Thomas, 2013). Wookey, Stackhouse, et al. (2005) show the possibility of explaining *P* and *S* reflections from the lowermost mantle as due to the phase transition from bridgmanite to ppv. In a pyrolitic mantle, this, however, would lead to a velocity jump smoothed over a depth range probably not sufficient to explain the reflections from the D″ discontinuity (Catalli et al., 2009). A joint effect of a phase transition with lattice-preferred orientation (LPO) fabric developed in ppv would change the gradient of the expected velocity contrast across the D″ discontinuity, leading to a sharper discontinuity (Ammann et al., 2010), and the alignment of ppv would then also be observable through directional variation of amplitudes and polarities of the reflected waves (Thomas et al., 2011; Wookey, Stackhouse, et al., 2005).

Deformation experiments have shown that ppv may develop LPO in the lowermost mantle (Merkel et al., 2006, 2007; Miyagi et al., 2010; Walte et al., 2009; Yamazaki et al., 2006). Compared to bridgmanite, the ppv structure seems to easily acquire an LPO (Goryaeva et al., 2016; Lay, 2015 and reference therein). At least four slip systems for ppv have been proposed (Merkel et al., 2006; Miyagi et al., 2010; Walte et al., 2009; Yamazaki et al., 2006). (001) slip, parallel to the CMB, predict the horizontally polarized *S* wave, SH, faster than the vertically polarized *S* wave, *SV*, for horizontal propagation at all azimuths, while both (100) and (010) show azimuthal anisotropy with alternation of *SH* and *SV* fast polarizations (Wookey & Kendall, 2007). Fabric developed by MgO is also a good candidate for explaining deep Earth seismic anisotropy (e.g., Karato, 1998; Karki et al., 1999; Long et al., 2006; Yamazaki & Karato, 2007). Shape-preferred orientation (SPO) of partial melt, possibly due to remnants of subducted oceanic crust or reaction products between core and mantle (e.g., Fouch et al., 2001; Kendall & Silver, 1998), is another alternative (or complementary) mechanism.

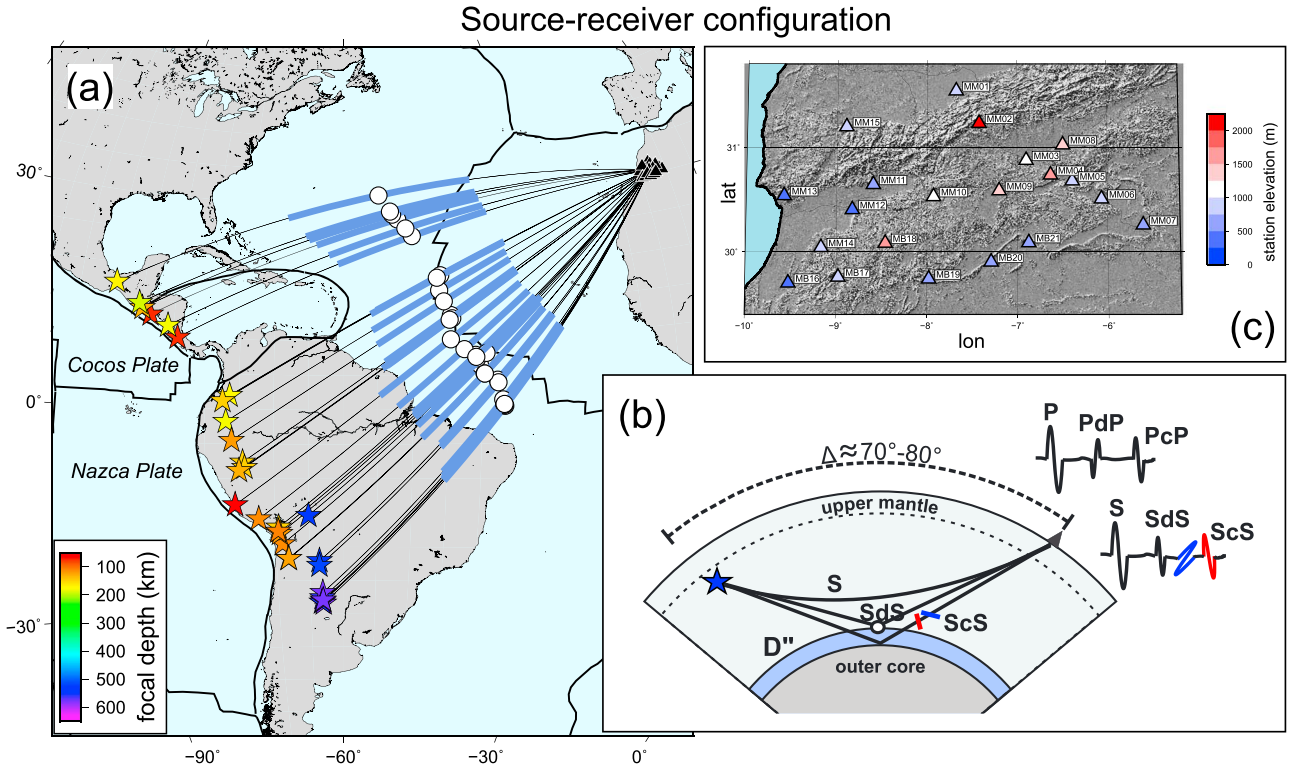

Figure 1. (a) Sources, receivers, and great circle paths used in this study. The central Atlantic Ocean is sampled using recordings from the Morocco-Array and earthquakes located along the Cocos and Nazca subduction zones. *ScS* paths are shown in blue and *PdP*/*SdS* reflections as white dots for a D″ discontinuity in a 1D velocity model (PWDK; Weber & Davis, 1990). (b) Schematic illustration of the deep mantle seismic phases used to detect and measure reflections and splitting parameters in the lowermost mantle. (c) Morocco-Array configuration and stations elevation, color coded with respect to the central station (MM10), used in the array analysis. The topography of the Anti-Atlas is also shown.

Discriminating between these different causes for generating anisotropy, deformation mechanism, and slip systems is important since they provide information on microstructures, heterogeneities, mineralogy, rheology, and dynamics of the deep Earth. One of the problems in studying the deep mantle is often the poor azimuthal coverage of travel paths for seismic waves required to infer a more general style of anisotropy with a lower degree of symmetry than transverse isotropy. By combining different methods along a given raypath direction, we might be able to compensate the lack of crossing paths. Here we propose a joint approach to study seismic anisotropy in the lowermost mantle by looking at both reflected waveform polarities and splitting from lower mantle seismic phases. We aim to test the hypothesis that this allows one to distinguish between different scenarios that cause anisotropy.

As a test region for our method, we chose the lowermost mantle beneath the central Atlantic Ocean, where the western border of the large low-shear-velocity province (LLSVP; Garnero et al., 2016; Lay, 2015) beneath Africa is located. Using *P* waves, Weber and Körnig (1990, 1992) found a seismic reflector at a depth of about 250–300 km above the CMB in this region. Based on *Sdiff* and *ScS* splitting and assuming a vertically transverse isotropic (VTI) medium, Garnero, Moore, et al. (2004) and Moore et al. (2002, 2004) infer a distance-dependent weak anisotropy, with fast polarization mixed between the *SH* and *SV* components, although strong azimuthal anisotropy might still be the cause for their observations.

2. Data and Observations

Waveforms sampling the lowermost mantle beneath the Atlantic Ocean come from 21 three-component seismic stations of a temporary array deployed in Morocco in the period 2010–2013 (Spieker et al., 2014). We use 30 earthquakes with foci located along the Cocos and Nazca plate subduction zones, beneath Central and North America, respectively (Figure 1a). The depths of the events range from 54 to 587 km. A list with all the used events is available in the supporting information (Table S1). Epicentral distances

range from 70° to 80°, which is the optimum distance to perform our analysis for two reasons: (a) within this distance range the reflection coefficient of *P* and *S* waves is large enough to be able to see reflections from the lowermost mantle (Cobden & Thomas, 2013; Weber, 1993) and (b) it allows us to correct the *ScS* splitting measurement for upper mantle anisotropy using other seismic phase such as *S* and *SK*(*K*)*S*, since they have roughly the same path in the upper mantle (Nowacki et al., 2011; Wookey, Kendall, et al., 2005). Reflection points and raypaths beneath the Atlantic are shown in Figures 1a and 1b. In total, we have an azimuthal coverage of about 40°. All data were filtered using a butterworth band-pass filter with corner frequencies of 1–3 to 10–15 s for the *P* waves and 3 to 15–25 s for the *S* waves.

We use array analysis (e.g., Rost & Thomas, 2002; Schweitzer et al., 2012) to detect reflections from the lowermost mantle since their amplitude is generally small. To distinguish between the different seismic waves arriving at the array and inspect their polarities, we use vespagrams, as shown in Figure 2 for *P* and Figure 3 for *S* waves. For the *S* waves we only use the transverse component. Following Jacobeit et al. (2013), a static correction was applied before stacking to correct for local structures and topography beneath the array (Figure 1c), which would otherwise affect our estimations of slowness and back azimuth.

Several of the analyzed vespagrams clearly show an arrival that agrees with a D″-reflected wave: Seismic phases *PdP* and *SdS* from such a reflector have their slowness values and traveltimes between the two main phases *P* (*S*) and *PcP* (*ScS*; Weber & Davis, 1990), and the examples in Figure 2 show two of the events with *PdP* and those in Figure 3 for the *SdS* arrivals. Further data are shown in Figures S1–S3 of the supporting information. The associated traveltime and slowness values place this reflector at the top of the D″ region (Bullen, 1950) in this area, with a lateral extent of around 1,500 km from NW to SE. The Fresnel zone for the appropriate period range at this depth is ~130 × 260 km (2° × 4°) for 1-s *PdP* and 230 × 460 km (3.5° × 7°) for 6-s *SdS* waves (Weber, 1993).

By inspecting the polarities of these reflected phases, we see cases where the *PdP* phase has either the same (positive) polarity or opposite (negative) polarity with respect to *PcP* and *P* (Figure 2). Figure 2a shows an example of *PdP* with the same-polarity (blue arrows) up-down lobes wavelet as *PcP*. A direct comparison with the more complex *P* wavelet is more difficult in this case. In contrast, Figure 2b illustrates an example of *PdP* with a wavelet that consists of up-down lobes that is opposite (red arrows) to the down-up wavelet shown by both *PcP* and *P* waves. Due to the potential amplitude and signal distortion of the nonlinear fourth-root stacking used in the vespagram (Rost & Thomas, 2002), we also compute linear vespagram and beams to further verify the polarity of our waves (Figure S1) and to enable a comparison also with the *P* wavelet. These linear vespagrams confirm the observation of the *PdP* polarity compared to *PcP* and *P*. We usually use, however, the *PcP* phase for this purpose as it has a similar takeoff angle and travel path as *PdP* and it is generally less complex than the *P* phase (which often has significant reverberations and multiples in its coda).

The observed negative polarity cannot be due to a focal mechanism since the *PdP* phase leaves the source with a takeoff angle between *P* and *PcP*, which both show the same polarity (Figure 2b). A source-related cause for the *PdP* reversal polarities could only happen close to nodal planes, which would also imply that the radiated energy of the *P* waves would be very small, while in our cases we do see a clear signal for these main phases. The *SdS* arrivals always show the same (positive) polarities when compared to *ScS* and *S* (Figure 3), and *SdS* amplitudes are usually larger than *PdP*. Observation of *PdP* and *SdS* polarities per events are listed in Tables S2 and S3.

We do not try to explain the variation of the *PdP* and *SdS* amplitudes as due to anisotropy, since too many factors would affect the amplitude estimation, such as attenuation, scattering in the lowermost mantle, and topography of the reflector, which would make the interpretation nonunique. Therefore, our analysis will only consider polarities. Overall, we detect an azimuthal/distance dependency of the reflected *P* wave polarity and no variation in the reflected shear wave polarities.

The stacking procedure used in producing vespagrams usually assumes that the energy travels along the great circle path. Because of 3D structures and reflector topography, however, the energy can also travel out of plane (e.g., Schumacher et al., 2018; Schumacher & Thomas, 2016). Therefore, we also performed slowness-back azimuth analyses that allow the detection of out-of-plane reflections (e.g., Rost & Thomas, 2002). This directional information must be considered when interpreting the azimuthal variation of seismic properties as due to anisotropy since the point of reflection and the local azimuth at the reflection point

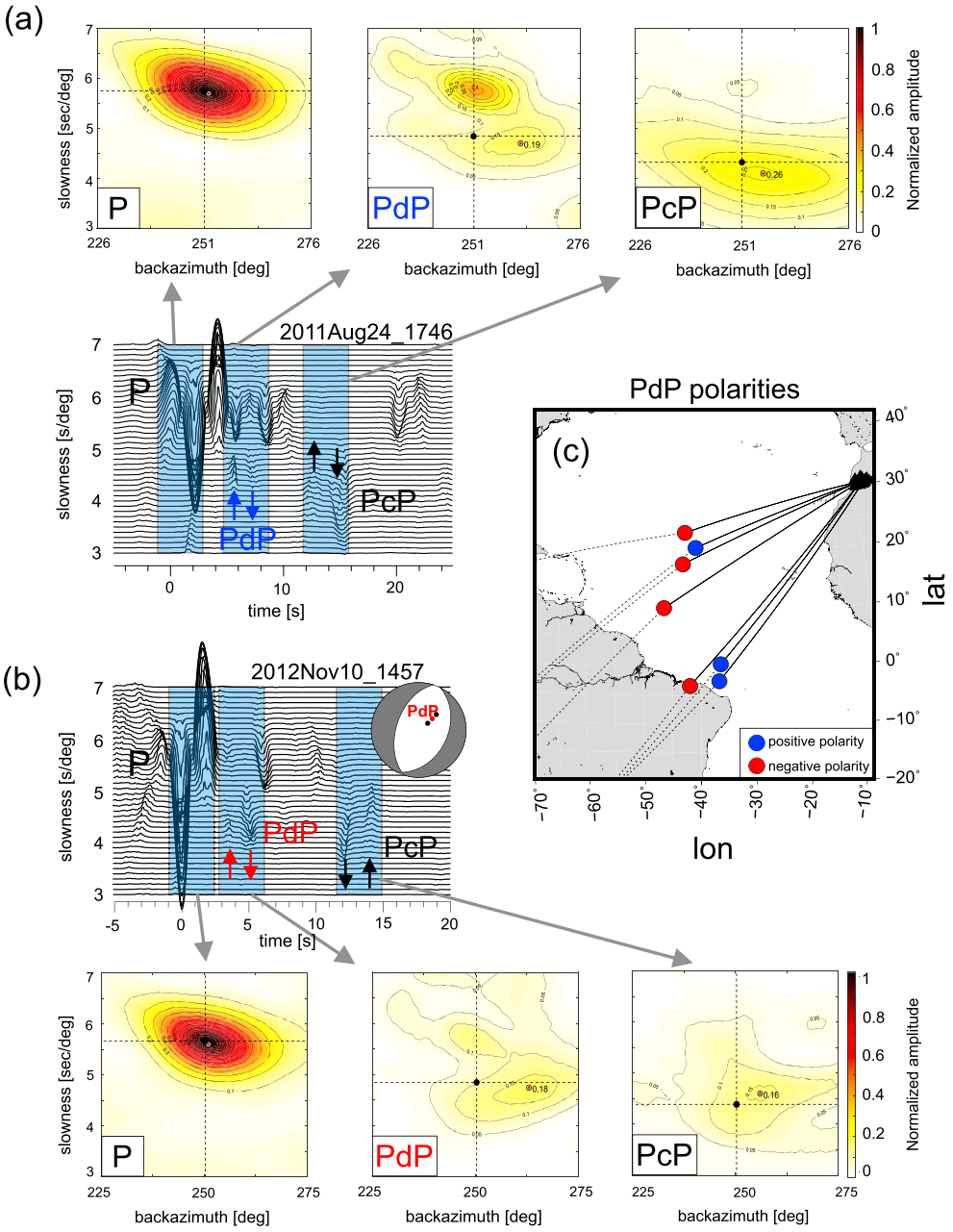

Figure 2. (a) Fourth-root vespagram for an example of *PdP* observation for the event 2011Aug24_1746. The blue arrows in the vespagram indicate that the *PdP* wavelet has the same (i.e., positive) up-down polarity compared to *PcP* (black arrows). Note that due to *P* waveform complexity, using the polarity of the *P* wave for comparison with *PdP* is difficult. The slowness-back azimuth plots indicate arrival directions of the *P*, *PdP*, and *PcP* waves, within time windows given by the gray areas in the vespagram. The dashed horizontal and vertical lines represent the theoretical slowness and backzimuth values. (b) As in (a) but for a negative polarity *PdP* (opposite polarity to *P* and *PcP*), event 2012Nov10_1457. The focal mechanism for this event is also given, with the directions of radiation for *P*, *PdP*, and *PcP* indicated. The red arrows indicate opposite polarity of *PdP* (up-down) with respect to *PcP* polarity (down-up) shown with black arrows. (c) Location of the *PdP* reflection points after back projections (see text).

needs to be known. Indeed, as we shall see later, anisotropy can cause variation of amplitude and polarities of reflections within a few degrees of azimuth.

In our data set we observe deviations up to 12° in back azimuth for the seismic phases reflected from the *D″* discontinuity (*PdP* and *SdS*) and also for the waves reflected from the CMB, that is, *PcP* and *ScS*. The main

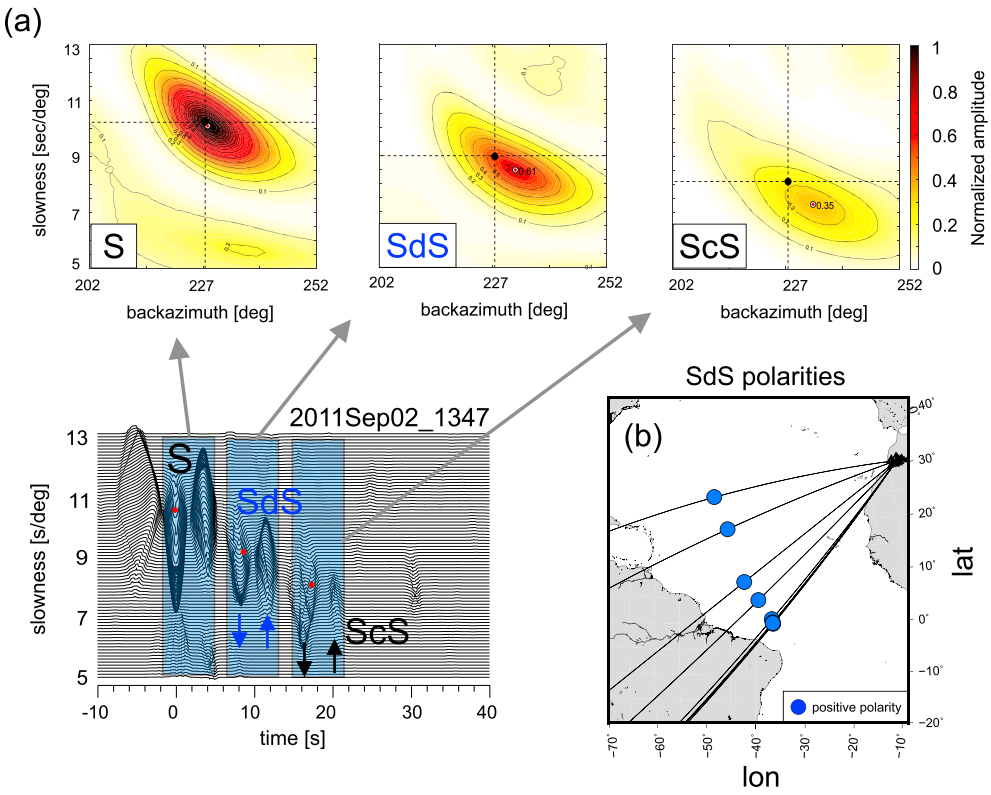

Figure 3. (a) Fourth-root vespagrams and slowness back azimuth analysis for the tangential component for an example of *S*, *SdS*, and *ScS* waves (event 2011Sep02_1347). In the slowness-back azimuth panels the dashed lines indicate theoretical values (from the PWDK model; Weber & Davis, 1990) for the indicated phases. Predicted arrivals for *S*, *SdS*, and *ScS* are also indicated in the vespagram as red spots. Time windows for the slowness-back azimuth plots are indicated as gray regions in the vespagram. The blue arrows in the vespagram indicate that the *SdS* wavelet has the same polarity compared with *ScS*. (b) Reflection points and great circles paths of *SdS*.

phases *P* and *S*, however, travel almost undisturbed along the great circle path connecting the source and receiver (Figures 2 and 3). These deviations could indicate either heterogeneities in the lowermost mantle or topography of the reflectors as pointed out by Weber (1993) or Thomas et al. (2002). In this work, we do not attempt to discriminate between the two causes for the out-of-plane reflections in our region, we merely use this information for estimating the reflection points and azimuths.

Following Schumacher and Thomas (2016), we use a ray tracer to back-project the reflected out-of-plane waves to the location in the lowermost mantle that best explain the observed slowness, back azimuth, and traveltime of seismic phases. For this calculation, every grid point (1° spacing) between 800 km and the CMB (in 10-km-depth interval) for model ak135 (Kennett et al., 1995) is considered as the reflector, and the point that gives the smallest traveltime difference is taken as the reflector depth. Geographical locations of the reflection points, after the back projection, are shown in Figure 2 for the *PdP* phases. Since we do not observe azimuthal variations of the *SdS* polarity (Figure 3), back projection of these reflection points does not change our interpretation of the anisotropy. Moreover, as we shall see later, the prediction of *S* reflection polarities does not often show strong azimuthal variations.

The average depth of the reflector is found to be around 2,650 ± 60 km. A 250-km-thick D″ region beneath the central Atlantic Ocean is in good agreement with previous estimates of a reflector in the same region (Weber & Körnig, 1990, 1992; Wysession et al., 1998) and in the North Atlantic Ocean (Wallace & Thomas, 2005), and it predicts the observed traveltime and slowness of *SdS* phases, as shown in Figure 3.

For the second approach to measure seismic anisotropy, we use differential splitting measurements *S-ScS* to estimate splitting parameters and correct for upper mantle anisotropy (Wookey, Kendall, et al., 2005). In this technique the correction for upper mantle anisotropy is performed by taking independent estimates of

source- and receiver-side anisotropy performed on the *S* and *SK*(*K*)*S* phases, respectively. In particular, the analysis is implemented based on the following steps: (i) The receiver-side anisotropy is measured on the *SK*(*K*)*S* waves (assuming a negligible lowermost mantle contribution), or the correction is taken from the literature. (ii) The source-side anisotropy is measured from the *S* waves, after correcting for the receiver-side anisotropy. (iii) The lowermost mantle anisotropy is then estimated on the *ScS* waves after removing the receiver side and before the application of the source-side anisotropy, to preserve the order of the splitting operators (Wookey, Kendall, et al., 2005; Wolfe & Silver, 1998). An example of *ScS* wave splitting observation is shown in Figure 4a, where the north component of the *ScS* motion is clearly delayed with respect to the east component. The *S* wave shows a smaller splitting with the north component leading the east one. The entire splitting analysis was carried out using Shear-wave Birefringence Analysis (SHEBA; Wuestefeld et al., 2010), which applies the minimum eigenvalue technique (Silver & Chan, 1991) on multiple time windows (Teanby et al., 2004) to estimate a pair of splitting parameters that best linearize an initial elliptical particle motion. SHEBA also allows to directly correct for receiver- and source-side contributions.

Measurements for the receiver side were taken from previously published multiazimuthal *SK*(*K*)*S* splitting beneath the High Atlas and Anti-Atlas in Morocco (Miller et al., 2013). We measure source-side splitting along the Nazca-Cocos subduction zone using *S* waves, after correcting the *S* wavelets for receiver-side anisotropy. One example of an S splitting measurements is shown in Figure 4b. Further examples are shown in Figure S4 of the supporting information. As a test for our measurements, we compare the retrieved source polarizations with predicted particle motions computed, taking source parameters from the Global Centroid Moment Tensor catalog (Dziewonski et al., 1981; Ekström et al., 2012). Following Nowacki et al. (2015, 2010), we project fast polarizations (φ), measured at the stations, back to the source region using the relation $\varphi'' = \mathrm{baz} + \mathrm{az} - \varphi$, where baz is the back azimuth and az is the azimuth at the source (Figure 4c). Because of similar slownesses and back azimuths, we assume that the events will have a single splitting operator at all stations, allowing us to stack the splitting measurements for each event (e.g., Wookey, Kendall, et al., 2005). A list with all the measured *S* splitting parameters, per event, is shown in Table S4. Our source-side splitting results show mostly trench-parallel fast polarizations, although trench-normal to trench-oblique fast directions are also detected in the northwestern path of South America, in the region of the Andean orocline, and in the southeastern part of the source region (Figure 4e). Depending on the raypaths, complexity in the pattern of fast polarization in this subduction region, with trench-parallel and/or trench-normal directions, is also found in previous studies (e.g., Anderson et al., 2004; Bock et al., 1998; Eakin, Long, Scire, et al., 2015; Eakin, Long, Wagner, et al., 2015; Hu et al., 2017; Idárraga-García et al., 2016; Lynner & Long, 2014b; Polet et al., 2000; Porritt et al., 2014; Russo & Silver, 1994; Walpole et al., 2017), although care should be taken when comparing different seismic phases propagating on different paths with different orientations, especially in such a complex multilayered anisotropic region (Eakin & Long, 2013; Eakin, Long, Wagner, et al., 2015; Lynner & Long, 2014b; Walpole et al., 2017).

In total, we collect 48 good-quality *ScS* splitting measurements across an area in D″ of about 1,500 km from NW to SE. Before the analysis, we remove receiver-side anisotropy estimations, and then we carry out the analysis of *ScS* splitting parameters while correcting for the source-side anisotropy (Wookey, Kendall, et al., 2005). One example of these measurements is shown in Figure 4d, and two other examples are given in Figure S5 of the supporting information. Observed delay times range from 0.4 to nearly 3 s, which fall into the commonly observed range for *ScS* splitting (Nowacki & Wookey, 2016). We back-project our *ScS* fast polarizations, measured in the geographic reference frame at the stations, into the ray reference frame for nearly horizontal propagating *ScS* waves in the lowermost mantle (Figure 4c) as in Nowacki et al. (2010). This allows us to have the fast polarizations as the angle away from the vertical in the plane normal to the *ScS* raypath.

We also attempted to perform splitting measurements on the *SdS* waves for the event shown in Figure 3, which has high-amplitude *SdS* wavelet. This analysis was not feasible for the other events due to the small amplitude of the *SdS* phase. The splitting values displayed by the *SdS* waves are comparable with those by the *S* waves, indicating that the two phases experienced same splitting and both are much smaller than the *ScS* splitting. Splitting measurements for *S*, *SdS*, and *ScS* waves for this event are shown in Table S5 and Figure S6. However, we did not include this event in the main analysis of the present work because in comparing the retrieved source polarization with that predicted using the Global Centroid Moment Tensor solution, we found discrepancies usually larger than 20°. Despite this, the result reinforces the

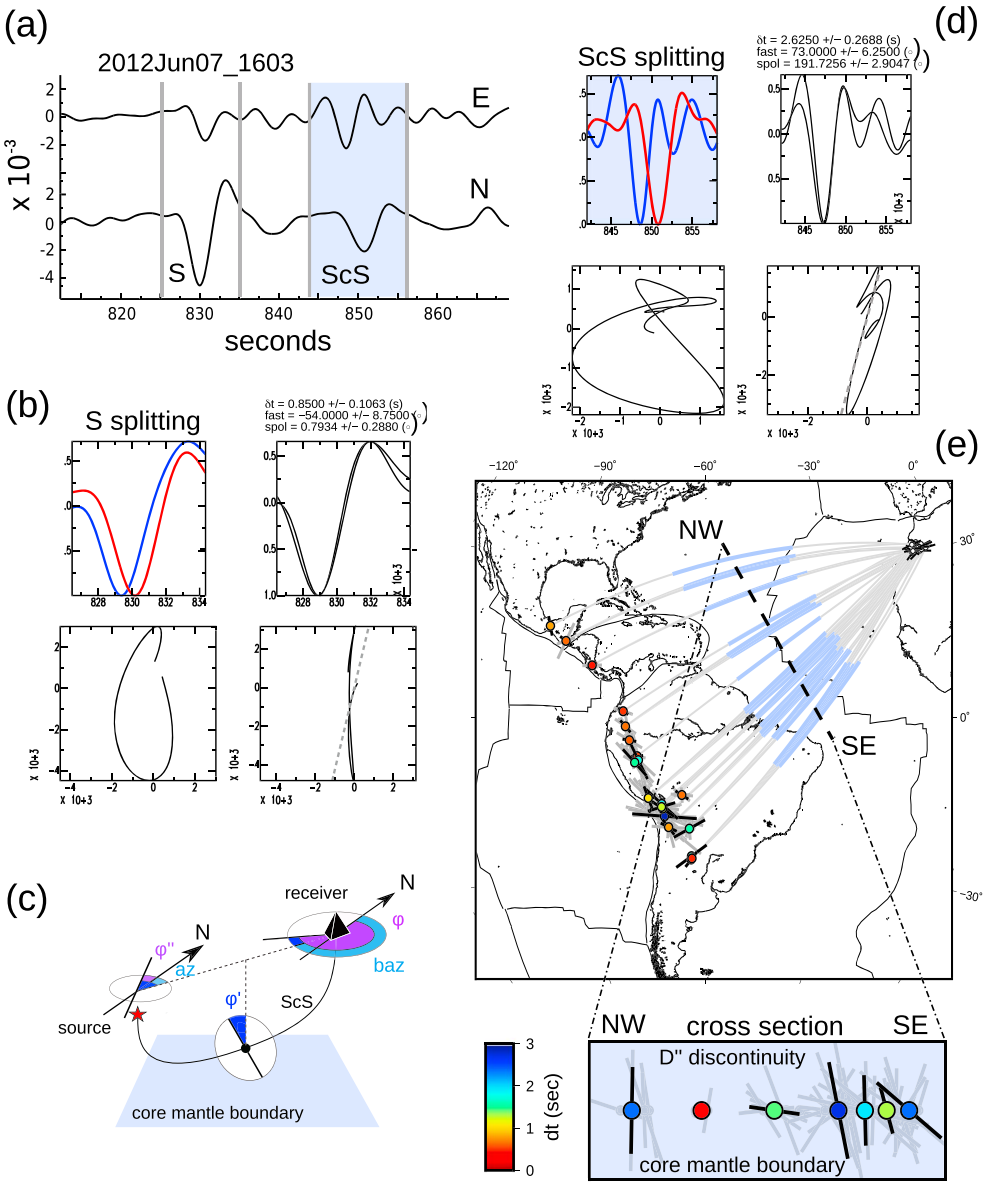

Figure 4. (a) Example of horizontal components of motion showing the *ScS* with a delay of the north component with respect to the east component for the event 2012Jun07_1603. (b) Fast and slow *S* wave and particle motion before and after splitting correction. The shaded gray line indicates the predicted source polarization for the event's focal mechanism from the Global Centroid Moment Tensor catalog (http://www.globalcmt.org). (c) Sketch to explain the projection of the fast polarizations, measured at the receiver (φ), to the source location for *S* waves (φ'') and to the lowermost mantle for *ScS* waves (φ'; after Nowacki et al., 2010). (d) Example of *ScS* splitting measurements showing fast and slow waves and particle motion before and after correcting for splitting. (e) Geographical location of the source-side splitting parameters (see text). Black bars show source-stacked results from single measurements (gray bars). Receiver-side splitting measurements from Miller et al. (2013) are displayed as black bars beneath stations in Morocco. The bottom panel shows a NW-SE cross section, along a plane roughly normal to the *ScS* paths (blue line). *ScS* fast polarizations are projected on this plane using the relation $\varphi' = \text{baz} - \varphi$. Thick black bars show stacked results; background gray bars show single-station measurements.

interpretation that the splitting that we measure on *ScS* wavelet is a relevant estimation of anisotropy confined to the D″ region below the D″ reflector.

To explore any azimuthal variation of the *ScS* splitting parameters across the sampled area and reduce the errors, we perform a weighted signal-to-noise ratio stacking (following Wolfe & Silver, 1998) of the 48 measurements, mapping our observations into seven subregions (see, e.g., Ford & Long, 2015, Ford et al., 2015;

Nowacki et al., 2010). Each of the stacked subregions includes measurements within a narrow range of raypath directions, that is, similar azimuths and slowness values. In Figure 4e, we show the stacked measurements along a NW-SE cross section normal to the *ScS* raypaths, with fast polarizations (φ') and color-coded delay times. The stacked measurements, per subregion, are also listed in Table S6. The fast polarizations show a complicated pattern with mainly *ScSV* leading *ScSH* in the NW part and *ScSH* fast polarization in the central area. An overall oblique SE dipping fast polarization is detected in the SE part.

Garnero, Moore, et al. (2004) observed an *SHdiff* slightly faster than *SVdiff* in our study region but, for a straightforward comparison with our results, the distance dependence of the splitting parameters in general anisotropic media must be considered. Distance-dependent splitting parameters for this region can be found in Moore et al. (2004) who used a compilation of *ScS* and *Sdiff* splitting measurements. Earlier work by Moore et al. (2002) found an overall *ScSV* faster than *ScSH*, which agrees with our observations. The complex observed pattern with azimuthal-dependent delay times and fast polarization directions rules out a simple VTI style of anisotropy beneath the studied region. Horizontal transverse isotropic or tilted transverse isotropic or even orthorhombic symmetry is likely responsible for the observed azimuthal variation of splitting parameters, as will be shown below.

3. Modeling Reflections and Splitting

As shown by Thomas et al. (2011), the azimuthal variation of polarities of waves reflected from the top of D″ can be used to investigate seismic anisotropy in the lowermost mantle. Here we extend this method to further investigate the effect of deformation of deep Earth minerals and resulting seismic anisotropy on both distance and azimuthal dependency of D″ reflection polarities. Additionally, shear wave splitting, the standard method used for seismic anisotropy studies (see Long & Silver, 2009; Nowacki, 2013, for reviews) is also expected to show a distance/azimuthal dependency of splitting parameters, even for high symmetry classes. We therefore perform modeling of reflection coefficients for reflected *P* and *S* waves (i.e., *PdP* and *ScS*) and shear wave splitting for different anisotropic media expected in the lowermost mantle.

In all our models, we assume an isotropic lower mantle over an anisotropic D″ region with a first-order flat discontinuity at the top. We model different scenarios by taking elastic constants and aggregate densities from Thomas et al. (2011). These elastic constants (Table S7) represent LPO textures of the main mineralogical phases expected in D″ (Irifune & Tsuchiya, 2015), such as bridgmanite and ppv, accommodating deformation along different slip systems (Mainprice et al., 2008; Miyagi et al., 2010; Walte et al., 2009; Yamazaki et al., 2006). We also tested a D″ region consisting of aligned tubular/oblate-shaped melt pockets in SPO fabric, surrounded by a homogeneous isotropic solid medium (e.g., Ford et al., 2015).

For each set of elastic constants and density aggregates, we compute reflection coefficients and splitting parameters for all ray propagation directions, which are unambiguously defined by incidence angle and azimuth with respect to deformation direction. Using the ray theory, we estimate the incidence angles of *PdP*/*SdS* and *ScS* waves reflecting atop D″ and the CMB interface, respectively. To do this, we refer to the 1D Earth velocity model PWDK (Weber & Davis, 1990) and use the TauP Toolkit (Crotwell et al., 1999) to convert epicentral distances in incidence angles. The reflection coefficients are computed following the theory developed by Fryer and Frazer (1984, 1987), Guest et al. (1993), and Chapman (2004) for arbitrary anisotropic media.

To compute splitting parameters for the *ScS* waves traveling in D″, we split the *ScS* raypath into the incident and reflected subpaths (Figure S7). This allows us to consider different splitting operators at either side of the core reflection point, especially for low symmetry classes such as tilted LPO of orthorhombic ppv. An effective splitting operator for the *ScS* wave is then computed by combining the splitting parameters of each path (Silver & Savage, 1994), considering an initial source polarization of 45° that ensures the same amplitude of *SH* and *SV* waves (Nowacki & Wookey, 2016). This ray-theory-based splitting calculation was performed using the Matlab Seismic Anisotropy Toolbox (MSAT; Walker & Wookey, 2012).

We use pole figures to present our results of the reflection coefficient and splitting modeling as a function of epicentral distance and azimuth with respect to the direction of deformation (Figure 5). Both *P* and *SH* reflections show characteristic features in their patterns, with positive and negative reflection coefficients occurring along both distance and azimuth. Thomas et al. (2011) only tested for one epicentral distance in

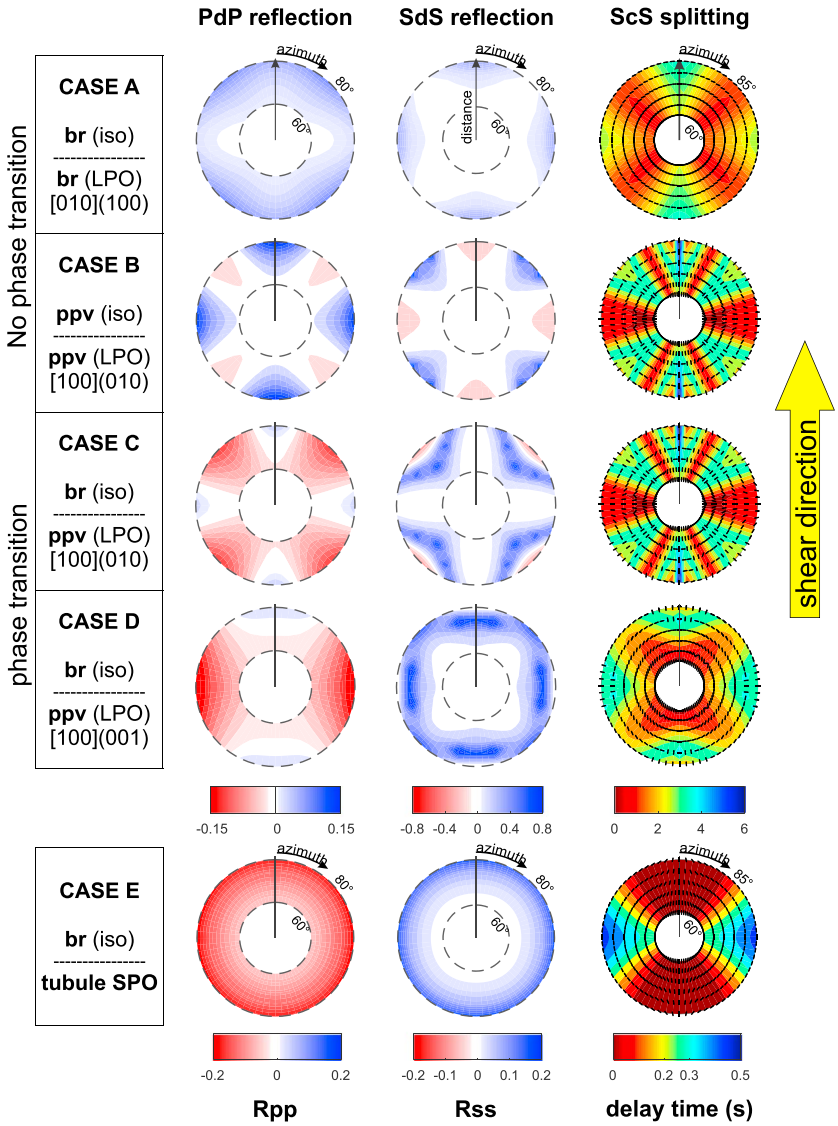

Figure 5. Pole figures showing the variation of reflection coefficient with azimuth and distances (60–80° for *PdP*/*SdS* reflections; 60–85° for *ScS* splitting) for the tested models. Azimuths are measured clockwise from deformation direction (solid vertical black line). The models include a material above D″ and another below D″ (indicated by the dashed lines). br = bridgmanite; ppv = postperovskite; LPO = lattice-preferred orientation; SPO = shape-preferred orientation. Different slip systems as indicated for each case. Color indicates reflection coefficient as given in the color bar and splitting times (for *ScS* splitting). Note that case E has a different color scale. Fast polarizations for the splitting (black tick marks) are given in the ray reference frame: where radial (tangential) means that *SV* (*SH*) is the fast polarization.

their models, and here we show that polarities of reflected waves can change also as a function of distance, not only as a travel direction.

The *P* waves seem to exhibit more polarity changes than do the *SH* waves, the latter also displaying larger reflection amplitudes, especially for positive reflections. As discussed by Cobden and Thomas (2013), this may lead to a bias toward positive *SdS* polarity observations, since the negative reflection coefficients of *SH* waves are only just above the detection threshold. Moreover, the negative SH reflection coefficients for almost all cases occur at the largest distances (>75°), where *S*, *SdS*, and *ScS* waves arrive close together, making the detection of such a polarity reversal in real data difficult to observe. In our data we observe positive-polarity *SdS* waves with larger amplitudes than *PdP* waves, but the *PdP* waves show positive and negative polarities within our narrow ranges of azimuth and distance. We also find white regions, which

indicate directions and azimuths where almost no energy is reflected. For some of the used models this feature occurs in a narrow range of directions between positive and negative lobes.

The modeled *ScS* splitting parameters also show a distance and azimuth dependence. Constructive interference between the splitting parameters of incident and reflected raypaths occurs along directions where fast polarizations have a similar dip at either side of the core reflection points, while destructive interference takes place where the fast polarization orientations differ (see Figure S7). The minima in delay times observed in cases B and C (at short distances along the plane perpendicular to the deformation direction) have their locations close to singular points in ppv, where the velocities of the two polarizations S1 (fast) and S2 (slow) are equal. These directions in anisotropic media, called acoustic axes, are also responsible for the abrupt changes in fast polarization directions along neighboring raypaths (Crampin & Yedlin, 1981).

The pattern shown by the pole figures of reflection coefficients and splitting parameters (Figure 5) allows us to distinguish between different scenarios by using the joint information of reflections and splitting: The scenarios without a phase transition, that is, cases A and B, can be distinguished by one type of measurement, since only case B predicts variations between positive and negative polarities of reflected waves as observed by our *P* waves and the splitting behavior in both cases is different. On the other hand, cases B and C show the same splitting parameters, since both contain an LPO in ppv deforming along [100](010) in D″. This would mean no distinction between the two cases if one only uses splitting to probe lowermost mantle anisotropy. By additionally using reflections, however, there is an added information that allows us to distinguish between the two cases, since the mantle overlying D″ consists of either isotropic ppv or isotropic bridgmanite. A similar scenario is presented between cases C and D. Finally, we also show a horizontal transverse isotropic medium consisting of SPO of tubular molten pockets (case E) below isotropic bridgmanite. We find no variation of polarities of *P* and *S* waves reflections and a simpler form of splitting measurements. Also, the amplitudes of the reflection coefficient for *S* waves would be smaller than those in the other cases, and no amplitude variation with azimuth is expected. Due to the very small azimuthal variation of impedance contrast, the reflections show a VTI pattern, while the splitting reveals the actual horizontal orientation of the symmetry axis, although delay times seem very small, at least for the case shown here. We also considered MgO single-crystal elasticity (Karki et al., 1999) in our initial models, but this predicts negative values of the *SdS* reflection coefficient at almost all azimuths (0–360°) and distances considered here (60–80°), which is incompatible with our observations.

Our modeling shows that using reflections of *P* and *S* waves and splitting together opens the possibility of testing mineralogy, fabric, and phase transitions in the lower mantle and D″. While the orthorhombic symmetry of the ppv LPO fabric in cases B and C underlying an isotropic lower mantle shows differences in the reflection coefficient pattern, the differences in the slip system, accommodating deformation in ppv (cases C and D), do not show characteristic features in the reflections but in the splitting parameters.

In our study region, a visual inspection of the data already rules out some of the models. For instance, no negative and positive *P* reflections are predicted for cases A and E. Case B, while it can potentially explain our negative and positive *P* reflection polarities and both *SH* to *SV* fast polarizations, cannot match the always observed positive *SdS* polarities (Figure 2) since it predicts negative *S* wave reflections when we find positive *P* wave reflections. Cases C and D, which have a phase transition from randomly oriented bridgmanite to aligned ppv, might be a scenario for the lowermost mantle beneath the central Atlantic Ocean since there is a variation for reflection coefficients and also splitting parameters and they can explain the positive *S* wave polarities. We find, however, that none of the cases in Figure 5 can fully explain our data.

It is possible that the anisotropy is tilted and any rotation of the models can change the reflection and splitting patterns. A rotation around the vertical axis would still result in the same reflection coefficient and splitting pattern and only change the deformation direction. This would allow a search for the deformation directions that best explain the observations. On the other hand, a rotation of the models around a horizontal axis would imply a tilted shear plane along which SPO/LPO occurs. For a proper discrimination of a given set of plausible models matching our observations, we perform a grid search by rotating the elastic constants of each model around the Cartesian axes (Nowacki et al., 2010). For each rotation, we compute reflections and splitting and we jointly compare them to the observations, only retaining the models that fit at least the 68% of each type of observation (i.e., *PdP*, *SdS*, and *ScS*). The misfit criterion for the reflection was represented by a binary comparison (either matching the polarity or not) of each *PdP* and *SdS* observation, while

for the splitting we only keep models which are compatible with the measured *ScS* fast polarization direction. We neglect delay times, as they are suggested to be an inaccurate estimate of anisotropy strength in ray-theory-based modeling of shear waves splitting and tend to underestimate the amount of anisotropy (Nowacki & Wookey, 2016). Moreover, also the trade-off between the thickness of the anisotropic layer and the strength of the anisotropy has to be considered.

None of the rotation of cases A, B, and E is able to reproduce the variability shown by the data, implying that a purely deformational fabric transition or SPO is unlikely a scenario for the observed anisotropy in the lowermost mantle beneath the central Atlantic Ocean. Of our over 250,000 starting models, considering all the possible aforementioned rotations, only about 300 models sufficiently explain at least 68% of our observations. We find that the observed azimuthal-distance variation in *PdP* polarity greatly narrows down the number of possible candidates to only 16 models corresponding to rotation of cases C and D (Figure S8), therefore showing the importance of relocating reflections that travel out of plane. *SdS* is reducing the solution space less strongly, since reflection polarities are always positive in our data set.

These 16 possible candidates that fit the highest number of observations have their shear plane roughly 90° apart from each other but due to the orthorhombic symmetry in ppv, the *P* and *S* wave anisotropy looks very similar (Figure S8). However, because case D displays subvertical shear planes with subhorizontal deformation and slip direction (resembling a strike-slip-like setting), while case C has less steep shear planes with subhorizontal slip directions and the lowest misfit, we consider the latter deformation scenarios as more plausible for being responsible for the observed anisotropy in our study region (Figure 6a).

From the distribution of the fitting models of case C (Figure S8), we computed an average best fit model with a tilted (36° ± 16°) shear plane dipping ESE (110° ± 20° from north) with subhorizontal (12° ± 9°) NE deformation/slip direction (36° ± 2° from north), as shown in Figure 6b. The deformation direction trending roughly SW-NE at this location and depth agrees with predictions of global mantle flow by Simmons et al. (2009). Their model, based on tomographic imaging, shows horizontal NE flow beneath the Atlantic between downwelling beneath Central and Southern America and upwelling beneath West and South Africa (Figure 6b).

4. Discussion

By using a combined approach of reflection polarities and splitting of seismic phases sampling D″, we can better constrain lowermost mantle anisotropy. To date, our knowledge about mantle deformation and anisotropy mostly relies on shear wave splitting studies. *P* wave anisotropy in the deep Earth has not been extensively investigated. A first effort in using *P* and *S* wave reflections to infer anisotropy in the deep mantle was undertaken by Thomas et al. (2011) using a variation of azimuths. This allowed us to distinguish between different scenarios, but it needed a variety of travel directions of waves in D″.

The approach presented in our study combines reflection polarities of *P* and *S* waves and splitting of seismic waves in D″ without the need for several azimuths but allows the use of data from only one azimuthal direction. Many D″ regions can be tested only by one source-receiver combination for reflections of the D″ structure, which leaves ambiguity with regard to the causes of the reflector. Combining reflections with splitting measurements for the same region, however, allows a discrimination between models, even if the spitting and reflection paths are different. Extending the reflection modeling to converted reflections (*PdS* or *SdP*) would also allow us to explore reflections coefficients at shorter distance ranges that would extend the seismic coverage of D″ and allow us to explore anisotropy in new regions.

Our observations of reflection coefficients and splitting results suggest a complex style of anisotropy in the D″ region beneath the central Atlantic Ocean. The *SdS* reflections show a simple pattern, that is, only positive polarities, while the *PdP* wave polarities exhibit a distance and azimuthal dependence. Only positive *S* wave reflection coefficients are expected for a model with a phase transition from bridgmanite to ppv (case D) or bridgmanite to aligned bridgmanite (case A) and for case C except for the largest distances. So *S* waves alone would not allow us to distinguish between cases A, C, and D.

The *PdP* reflection polarities for an isotropic ppv phase transition would be negative (Wookey, Stackhouse, et al., 2005) and would imply the same amount of reflected energy for all directions and likely small amplitude due to the smaller impedance across the bridgmanite-ppv phase discontinuity (e.g., Cobden et al., 2015).

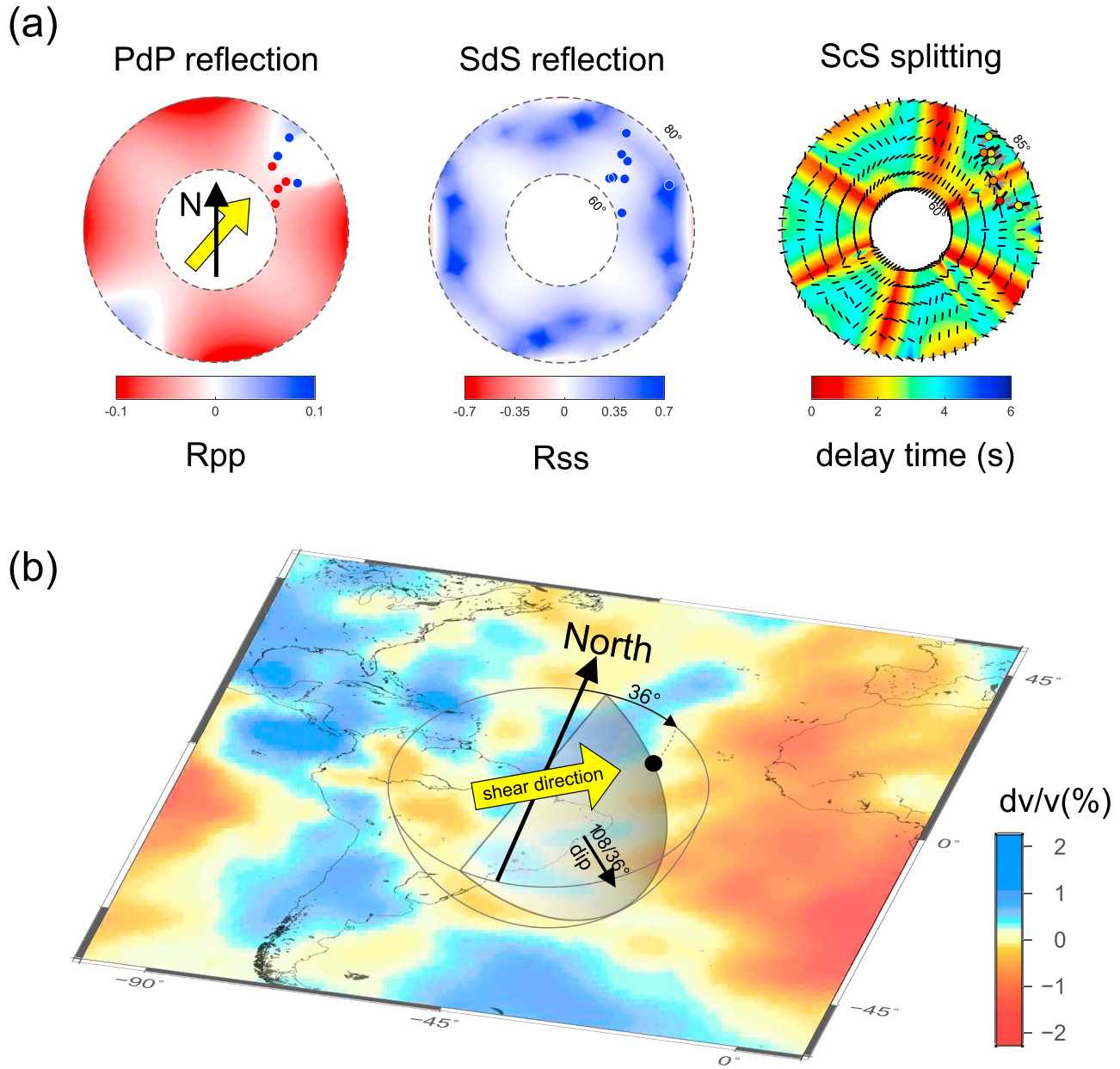

Figure 6. (a) Best fit model for our study region. The model corresponds to case C of Figure 5, with rotation of deformation direction by 36° from north and a tilted shear plane dipping ESE. To locate our measurements on the pole figures (scattered solid points, with fast polarization direction for splitting), we use the observed slowness-back azimuth values (Figures 2 and 3) and convert them into incidence angle and azimuth at the bounce point. (b) Schematic illustration of lower-hemisphere stereographic projection of best fit shear plane and deformation direction on top of a tomographic model (S40RTS; Ritsema et al., 2011). Solid black point indicates slip (shear) direction (36° from north), and black arrow indicates dip direction (108° from north) and inclination (36° from horizontal) of best fit shear plane.

For aligned ppv, on the other hand, the models predict variable polarities (cases B, C, and D). Alignment of ppv crystals might also lead to magnification or reduction of the reflection coefficient in certain directions and therefore could create strong *PdP* waves or cases where no *PdP* is observed. This might explain strongly variable amplitudes of especially *PdP* waves and also to a certain extent *SdS* waves as, for example, observed in Weber (1993), Thomas and Weber (1997), Kito et al. (2007), or Cobden and Thomas (2013) although scattering or topography may also be responsible for strongly variable amplitudes of *PdP* and *SdS* waves and absence of reflections from D″ (e.g., Scherbaum et al., 1997; Thomas & Weber, 1997). In addition, along these low-reflection coefficient directions, the energy is transmitted in the underlying

medium, and therefore, local amplitude variations of *PcP* and *ScS* may also be partly explained through anisotropy in D″.

Carrying out the comparison between the different models and our observations, we then find that a phase transition from randomly oriented bridgmanite to LPO fabric in ppv, with the deformation direction rotated by (36° ± 2°) clockwise from north, and subhorizontal slip plane (Figure 6a).

Our preferred model predicts a ppv alignment accommodated by the [100](010) slip system. The same slip system is found in paleosubduction regions (Nowacki et al., 2013) using shear wave splitting as well as by Thomas et al. (2011) for the D″ region beneath Eurasia and Caribbean, using reflections. Ford et al. (2015) infer the same slip plane using splitting measurements for a region located at the eastern edge of the African LLSVP.

Single-crystal anisotropic properties for ppv with horizontal (010) predict an azimuthal variation of fast polarization directions rapidly changing from *SV* to *SH* (Wookey & Kendall, 2007; Wookey, Stackhouse, et al., 2005), which fits our observations. In regions of presumed dominant horizontal flow in the deep mantle, Walker et al. (2011) find a good correlation between the elastic anisotropy predicted by a plasticity model of fabric accommodated by the (010) plane and the global seismic observations in regions of dominant fast vertically polarized shear waves. Based on theoretical calculations, the slip system [100](010) is easiest to deform in ppv (Goryaeva et al., 2015, 2016), making the layered structures of the ppv weaker than bridgmanite and highly anisotropic. Further and more realistic scenarios will be tested in future work, including deformation of multiphase assemblies with ppv and ferropericlase (e.g., Tommasi et al., 2018).

The observed complicated pattern in our splitting measurements is not surprising, given the postulated complexity of flow and deformation across the LLSVP borders (Romanowicz & Wenk, 2017). Cottaar and Romanowicz (2013) found that anisotropy near the southern edge of the African LLSVP is strong outside the anomaly, rotates or weakens at the edge, and seems to be absent inside the LLSVP. Our data sample the western edge of the African LLSVP, and it is not entirely clear where its edge is located. Our observations might aid in constraining the edge of the LLSVP western boundary beneath the Atlantic in future work.

Previous studies tested anisotropy near our study region: Garnero, Moore, et al. (2004) used diffracted *S* waves and find weak anisotropy with horizontally polarized *S* wave slightly faster than the vertically polarized *S* wave beneath the Atlantic. However, their study uses *Sdiff* waves with horizontal paths in D″, while the *ScS* waves in our study represent wide-angle reflections. Moore et al. (2004) measured *ScS* splitting in our study region and found a dominant *SV* faster than *SH* in the distance range 70–80°, in agreement with our measurements.

Nowacki and Wookey (2016) note that the distance must be considered for the interpretation of the splitting parameters, but in our results we find that the distance is less significant than the azimuth of the waves when only using the horizontal (nonrotated) cases. The splitting parameters along one azimuth are similar for all distances but can vary rapidly with changing azimuth. If, however, we rotate the models, the splitting parameters also vary with distance and not only azimuth. This behavior could possibly explain the strongly varying anisotropy found in the Pacific (e.g., Pulliam & Sen, 1998).

We find with our combination of reflection polarities and splitting parameters that a phase-transition-related discontinuity might be responsible for the observed reflections. Using the slowness, back azimuth, and traveltime of the waves, we find a reflector at depth around 2,650 km with small topography. A reflector at about the same depth was also found by Weber and Körnig (1990, 1992) using data from the bulletin of the International Seismological Center (ISC). Plate tectonic reconstructions, based on tomographic models, find fast velocities located at depths greater than 2,600 km in our study region, which is associated with an ancient subducted slab, Atlantis, residing at the CMB (van der Meer et al., 2010, 2018). The reflector found in our data set may represent the top of this slab, and the colder slab material could induce a phase transition from bridgmanite to ppv (Chaloner et al., 2009; Hernlund et al., 2005; Hutko et al., 2006), but because we find moderate topography, the temperature variation in the region might be small. A purely thermal slab would create a different signature, in that the reflector would not be sharp and therefore not visible with short-period waves (Thomas et al., 2004). To create a sharp reflector, as seen in our data set, one possibility is the alignment of minerals in the slab. In our modeling we tested scenarios with mineral alignment without a phase change, but their signature is

different from our observations (see Figure 5, cases A and B). Also, aligned inclusions (i.e., case E) do not show any pattern as seen in our data. Therefore, based on our observations and modeling, we assume that we are observing a phase change from bridgmanite to aligned ppv in the studied region.

Topography of the top of the slab might deviate the seismic waves and could be responsible for the observed out-of-plane reflections in our region. Sidorin et al. (1999a, 1999b) discussed the effect of lateral variation in temperature on the depth of a phase change in the deep mantle, and its impact on the height and topography of the D″ discontinuity and great circle path deviation of up to 12° for deep mantle D″ reflections were also reported by Weber (1993) as indication of topography of the D″ reflector. Topography of the D″ reflector was also found in previous studies sampling the Atlantic to the north of our region (e.g., Durand et al., 2018; Wallace & Thomas, 2005; Yao et al., 2015). Topography, however, should not change our interpretation of the polarity measurements for the anisotropy since previous modeling (e.g., Thomas & Weber, 1997) has shown in a 2D case that there is a negligible effect of topography on polarity of the reflected waves, although 3D modeling should be tested in the future to fully demonstrate this.

One possibility could be that our study covers a strongly heterogeneous region. A modest degree of 3D heterogeneity beneath the Atlantic was found by Garnero, Moore, et al. (2004). Given the complexity of the region investigated, located between subduction from South America slabs and the large low velocity region beneath Africa, these strongly heterogeneous structures as a cause for the observed pattern in polarity and splitting cannot be absolutely ruled out.

However, by assuming the simplest case of a homogeneous anisotropy model with the same mineralogy for our sampled region, the amount of anisotropy predicted by our final model ranges from 0.6% to 2.3% for a uniform 300-km D″ thickness that we constrain with our reflections. The estimated amount of anisotropy for the studied region falls into the observed range (0.5–3%) for those below subduction zones (Nowacki et al., 2011). This represents a lower bound to the estimated anisotropy in our studied region as it trades off with the assumed thickness of the anisotropic layer. Karato (1998) suggested that the anisotropy is more likely to be confined in the top part of horizontally sheared subducted cold slabs residing at the CMB. Although we are able to constrain the onset depth of the deformed anisotropic layer by using reflections from the top of such a layer (i.e., *PdP* and *SdS* waves), an estimation of its vertical thickness and therefore the thickness of the anisotropic region is not possible with our method, and detailed waveform studies are required to solve the vertical extent of the anisotropy (Moore et al., 2004), taking into account also the wavelengths of the waves used to probe the anisotropy. However, the example of *SdS* splitting (Figure S6) seems to suggest that the measured splitting of *ScS* results from within the D″ reflector. The presence of additional reflections within D″ could indicate a lower boundary of the anisotropic region if the anisotropy is due to aligned ppv (Ammann et al., 2010; Thomas et al., 2011) since the double-crossing model (Hernlund et al., 2005) predicts the backtransformation of ppv into bridgmanite. We did not find secondary reflections in our data set, but using other epicentral distances and more data coverage could help to identify lower reflectors, if they are present.

5. Conclusions

We use a combination of splitting measurements of *ScS* waves and polarities of reflected *P* and *S* waves from the top of the D″ region to constrain anisotropy in the D″ region beneath the central Atlantic. The aim was to find out whether, using a combination of two methods, we could relax the criterion of using several azimuths to better constrain the style of anisotropy and the associated mineralogy.

Using array analysis, we found a reflector in the lowermost mantle beneath the central Atlantic Ocean at depth of about 2,650 km. This reflector shows azimuthal anisotropy as observed from *PdP* polarities that vary with distance and travel azimuth. The *SdS* waves, in contrast to the variable *PdP* wave polarity, shows a much simpler behavior with no azimuthal and distance polarity dependence. We find out-of-plane behavior of *PdP* and *SdS* waves and back-project the waves to their points of reflection since the true reflection point is needed to constrain the anisotropy models.

We find variable splitting in the D″ region using *ScS* waves corrected for upper mantle anisotropy in the source and receiver regions. The sampled area shows vertical fast polarization in the northwestern part varying to horizontal and tilted fast polarization in the central and southeastern regions, respectively. The

splitting parameters found with our analysis rule out a simple VTI media for the investigated region, given their azimuthal variations.

Using the ray theory to model reflection coefficients for *P* and *S* wave D″ reflections and *ScS* splitting measurements, we find that a complicated pattern of reflections and splitting is expected. For example, the LPO of orthorhombic minerals such as bridgmanite or ppv will lead to azimuthal and distance dependency of polarities and splitting parameters in a different manner. Taking both observations, it is possible to probe seismic anisotropy in the deep Earth and distinguish between different mineralogical scenarios. By assuming a homogeneous anisotropy scenario with the same mineralogy and deformation style for our sampled region, our preferred model suggests a phase transition from isotropic bridgmanite to LPO fabric developed in ppv. To match the observations, we infer a subhorizontal (12° ± 9°) SW-NE trending deformation direction (36° ± 2°) and tilted shear plane (36° ± 16°) dipping ESE with 110° ± 20° from north.

We show that the joint information of *P* and *S* wave reflections together with results from *S* wave splitting along one raypath direction compensates for the lack of crossing raypaths usually needed to constrain causes for general azimuthal anisotropy and allows us to constrain mineralogy and deformation. Note that the splitting does not even have to be along the same raypath as the reflections. Extending the method to include other wave types, such as *SKS*/*SKKS* splitting or converted waves (*PdS* or *SdP*), could further reduce the need for azimuthal coverage of a region. This opens up the way for testing more regions for more general anisotropy and associated mineralogy.

Acknowledgments
We would like to thank the editor Martha Savage and two anonymous reviewers for helpful suggestions and comments that improved the clarity of the manuscript. This project has received funding from the European Union's Horizon 2020 research and innovation program under the Marie Sklodowska-Curie grant agreement 642029-ITN CREEP. Data were obtained from the Morocco-Array project funded under grant DFG TH1530/5-1 (https://doi.org/10.7914/SN/3D_2010). The data were processed using Seismic Handler (Stammler, 1993), SAC (https://www.iris.edu/hq/), and the Taup Toolkit (Crotwell et al., 1999). We thank Lina Schumacher for providing the code to backtrace the out-of-plane reflections in the lowermost mantle. The SHEBA program is available at https://github.com/jwookey/sheba. Maps were drawn using GMT (Wessel & Smith, 1995), and modeling of anisotropy was partially done using MSAT (Walker & Wookey, 2012).

References

Ammann, M. W., Brodholt, J. P., Wookey, J., & Dobson, D. P. (2010). First-principles constraints on diffusion in lower-mantle minerals and a weak D″ layer. *Nature*, *465*(7297), 462–465. https://doi.org/10.1038/nature09052

Anderson, M. L., Zandt, G., Triep, E., Fouch, M., & Beck, S. (2004). Anisotropy and mantle flow in the Chile-Argentina subduction zone from shear wave splitting analysis. *Geophysical Research Letters*, *31*, L23608. https://doi.org/10.1029/2004GL020906

Bataille, K., Wu, R. S., & Flatté, S. M. (1990). Inhomogeneities near the core–mantle boundary evidenced from scattered waves: A review. *Pure and Applied Geophysics*, *132*(1-2), 151–173. https://doi.org/10.1007/BF00874361

Bock, G., Kind, R., Rudloff, S., & Asch, G. (1998). Shear wave anisotropy in the upper mantle beneath the Nazca Plate in northern Chile. *Journal of Geophysical Research*, *103*(B10), 24,333–24,345. https://doi.org/10.1029/98JB01465

Brana, L., & Helffrich, G. (2004). A scattering region near the core mantle boundary under the North Atlantic. *Geophysical Journal International*, *158*(2), 625–636. https://doi.org/10.1111/j.1365-246X.2004.02306.x

Bullen, K. E. (1949). Compressibility-pressure hypothesis and the Earth's interior. *Monthly Notices of the Royal Astronomical Society, Geophysical*, *5*(9), 335–368. https://doi.org/10.1111/j.1365-246X.1949.tb02952.x

Bullen, K. E. (1950). An earth model based on a compressibility-pressure hypothesis. *Geophysical Journal International*, *6*, 50–59. https://doi.org/10.1111/j.1365-246X.1950.tb02973.x

Catalli, K., Shim, S. H., & Prakapenka, V. (2009). Thickness and Clapeyron slope of the postperovskite boundary. *Nature*, *462*(7274), 782–785. https://doi.org/10.1038/nature08598

Chaloner, J., Thomas, C., & Rietbrock, A. (2009). P- and S-wave reflectors in D″ beneath South-East Asia. *Geophysical Journal International*, *179*(2), 1080–1092. https://doi.org/10.1111/j.1365-246X.2009.04328.x

Chapman, C. H. (2004). *Fundamentals of seismic wave propagation*. Cambridge, UK: Cambridge University Press. https://doi.org/10.1017/CBO9780511616877

Cobden, L., & Thomas, C. (2013). The origin of D″ reflections: A systematic study of seismic array data sets. *Geophysical Journal International*, *194*(2), 1091–1118. https://doi.org/10.1093/gji/ggt152

Cobden, L., Thomas, C., & Trampert, J. (2015). Seismic detection of post-perovskite inside the Earth. In A. Khan & F. Deschamps (Eds.), *The Earth's heterogeneous mantle: A geophysical, geodynamical, and geochemical perspective* (pp. 391–440). Cham, Switzerland: Springer International Publishing.

Cottaar, S., & Romanowicz, B. (2013). Observations of changing anisotropy across the southern margin of the African LLSVP. *Geophysical Journal International*, *195*(2), 1184–1195. https://doi.org/10.1093/gji/ggt285

Crampin, S., & Yedlin, M. (1981). Shear-wave singularities in wave propagation in anisotropic media. *Journal of Geophysics*, *107*(3), 531–543. https://doi.org/10.1111/j.1365-246X.1991.tb01413.x

Crotwell, H. P., Owens, T. J., & Ritsema, J. (1999). The TauP toolkit: Flexible seismic travel-time and ray-path utilities. *Seismological Research Letters*, *70*(2), 154–160. https://doi.org/10.1785/gssrl.70.2.154

Durand, S., Thomas, C., & Jackson, J. M. (2018). Constraints on D″ beneath the North Atlantic region from *P* and *S* traveltimes and amplitudes. *Geophysical Journal International*, *216*(2), 1132–1144. https://doi.org/10.1093/gji/ggy476

Dziewonski, A. M., Chou, T.-A., & Woodhouse, J. H. (1981). Determination of earthquake source parameters from waveform data for studies of global and regional seismicity. *Journal of Geophysical Research*, *86*(B4), 2825–2852. https://doi.org/10.1029/JB086iB04p02825

Eakin, C. M., & Long, M. D. (2013). Complex anisotropy beneath the Peruvian flat slab from frequency-dependent, multiple-phase shear wave splitting analysis. *Journal of Geophysical Research: Solid Earth*, *118*, 4794–4813. https://doi.org/10.1002/jgrb.50349

Eakin, C. M., Long, M. D., Scire, A., Beck, S. L., Wagner, L. S., Zandt, G., & Tavera, H. (2015). Internal deformation of the subducted Nazca slab inferred from seismic anisotropy. *Nature Geoscience*, *9*(1), 56–59. https://doi.org/10.1038/ngeo2592

Eakin, C. M., Long, M. D., Wagner, L. S., Beck, S. L., & Tavera, H. (2015). Upper mantle anisotropy beneath Peru from SKS splitting: Constraints on flat slab dynamics and interaction with the Nazca Ridge. *Earth and Planetary Science Letters*, *412*, 152–162. https://doi.org/10.1016/j.epsl.2014.12.015

Ekström, G., Nettles, M., & Dziewonski, A. M. (2012). The global CMT project 2004–2010: Centroid-moment tensors for 13,017 earthquakes. *Physics of the Earth and Planetary Interiors*, *200-201*, 1–9. https://doi.org/10.1016/j.pepi.2012.04.002

Ford, H. A., & Long, M. D. (2015). A regional test of global models for flow, rheology, and seismic anisotropy at the base of the mantle. *Physics of the Earth and Planetary Interiors*, *245*, 71–75. https://doi.org/10.1016/j.pepi.2015.05.004

Ford, H. A., Long, M. D., He, X., & Lynner, C. (2015). Lowermost mantle flow at the eastern edge of the African large low shear velocity province. *Earth and Planetary Science Letters*, *420*, 12–22. https://doi.org/10.1016/j.epsl.2015.03.029

Ford, S. R., Garnero, E. J., & McNamara, A. K. (2006). A strong lateral shear velocity gradient and anisotropy heterogeneity in the lowermost mantle beneath the southern Pacific. *Journal of Geophysical Research*, *111*(B3), B03306. https://doi.org/10.1029/2004JB003574

Fouch, M. J., Fischer, K. M., & Wysession, M. E. (2001). Lowermost mantle anisotropy beneath the Pacific: Imaging the source of the Hawaiian plume. *Earth and Planetary Science Letters*, *190*(3-4), 167–180. https://doi.org/10.1016/S0012-821X(01)00380-6

Fryer, G. J., & Frazer, L. N. (1984). Seismic waves in stratified anisotropic media. *Geophysical Journal of the Royal Astronomical Society*, *78*(3), 691–710. https://doi.org/10.1111/j.1365-246X.1984.tb05065.x

Fryer, G. J., & Frazer, L. N. (1987). Seismic waves in stratified anisotropic media—II. Elastodynamic eigensolutions for some anisotropic systems. *Geophysical Journal of the Royal Astronomical Society*, *91*(1), 73–101. https://doi.org/10.1111/j.1365-246X.1987.tb05214.x

Garnero, E. J. (2000). Heterogeneity of the lowermost mantle. *Annual Reviews of the Earth and Planetary Science*, *28*(1), 509–537. https://doi.org/10.1146/annurev.earth.28.1.509

Garnero, E. J., Maupin, V., Lay, T., & Fouch, M. J. (2004). Variable azimuthal anisotropy in Earth's lowermost mantle. *Science*, *306*(5694), 259–261. https://doi.org/10.1126/science.1103411

Garnero, E. J., McNamara, A. K., & Shim, S.-H. (2016). Continent-sized anomalous zones with low seismic velocity at the base of Earth's mantle. *Nature Geoscience*, *9*(7), 481–489. https://doi.org/10.1038/ngeo2733

Garnero, E. J., Moore, M. M., Lay, T., & Fouch, M. J. (2004). Isotropy or weak vertical transverse isotropy in D″ beneath the Atlantic Ocean. *Journal of Geophysical Research*, *109*, B08308. https://doi.org/10.1029/2004JB003004

Goryaeva, A. M., Carrez, P., & Cordier, P. (2015). Modeling defects and plasticity in $MgSiO_3$ post-perovskite: Part 2—Screw and edge [100] dislocations. *Phyisics and Chemistry of Minerals*, *42*(10), 793–803. https://doi.org/10.1007/s00269-015-0763-8

Goryaeva, A. M., Carrez, P., & Cordier, P. (2016). Low viscosity and high attenuation in $MgSiO_3$ post-perovskite inferred from atomic scale calculations. *Scientific Reports*, *6*(1), 34771. https://doi.org/10.1038/srep34771

Grand, S. P. (2002). Mantle shear-wave tomography and the fate of subducted slabs. *Philosophical Transactions of the Royal Society of London. Series A*, *360*(1800), 2475–2491. https://doi.org/10.1098/rsta.2002.1077

Grand, S. P., van der Hilst, R. D., & Widiyantoro, S. (1997). Global seismic tomography: A snapshot of convection in the Earth. *GSA Today*, *7*(4), 1–7.

Guest, W. S., Thomson, C. J., & Spencer, C. P. (1993). Anisotropic reflection and transmission calculations with application to a crustal seismic survey from the East Greenland Shelf. *Journal of Geophysical Research*, *98*(B8), 14,161–14,184. https://doi.org/10.1029/93JB01156

Hernlund, J. W., Thomas, C., & Tackley, P. J. (2005). A doubling of the post-perovskite phase boundary and the structure of the lowermost mantle. *Nature*, *434*(7035), 882–886. https://doi.org/10.1038/nature03472

Hirose, K. (2007). Discovery of post-perovskite phase transition and the nature of D″ layer. In K. Hirose, J. Brodholt, T. Lay, & D. Yuen (Eds.), *Post-perovskite, the last mantle phase transition*, *Geophysical Monograph Series* (Vol. 174, pp. 19–35). Washington, DC: American Geophysical Union.

Hu, J., Faccenda, M., & Liu, L. (2017). Subduction-controlled mantle flow and seismic anisotropy in South America. *Earth and Planetary Science Letters*, *470*, 13–24. https://doi.org/10.1016/j.epsl.2017.04.027

Hutko, A., Lay, T., Revenaugh, J., & Garnero, E. J. (2006). Seismic detection of folded, subducted lithosphere at the core-mantle boundary. *Nature*, *441*(7091), 333–336. https://doi.org/10.1038/nature04757

Idárraga-García, J., Kendall, J. M., & Vargas, C. A. (2016). Shear wave anisotropy in northwestern South America and its link to the Caribbean and Nazca subduction geodynamics. *Geochemistry Geophysiscs Geosystem*, *17*(9), 3655–3673. https://doi.org/10.1002/2016GC006323

Irifune, T., & Tsuchiya, T. (2015). 2.03 Phase transitions and mineralogy of the lower mantle. In G. Schubert (Ed.), *Treatise on geophysics* (2nd ed., pp. 33–60). Oxford: Elsevier.

Jacobeit, E., Thomas, C., & Vernon, F. (2013). Influence of station topography and Moho depth on the mislocation vectors for the Kyrgyz Broadband Seismic Network (KNET). *Geophysical Journal International*, *193*(2), 949–959. https://doi.org/10.1093/gji/ggt014

Kárason, H., & van der Hilst, R. D. (2001). Tomographic imaging of the lowermost mantle with differential times of refracted and diffracted core phases (*PKP*, *P*diff). *Journal of Geophyical Research*, *106*(B4), 6569–6587. https://doi.org/10.1029/2000JB900380

Karato, S. (1998). Some remarks on the origin of seismic anisotropy in the D″ layer. *Earth, Planets and Space*, *50*(11-12), 1019–1028. https://doi.org/10.1186/BF03352196

Karki, B. B., Wentzcovitch, R. M., de Gironcoli, S., & Baroni, S. (1999). First-principles determination of elastic anisotropy and wave velocities of MgO at lower mantle conditions. *Science*, *286*(5445), 1705–1707. https://doi.org/10.1126/science.286.5445.1705

Kendall, J. M. (2000). Seismic anisotropy in the boundary layers of the mantle. In S. Karato, A. Forte, R. Lieberman, G. Masters, & L. Stixrude (Eds.), *Earth's deep interior: Mineral physics and tomography from the atomic to the global scale*, *Geophysical Monograph Series* (Vol. 117, pp. 133–159). Washington, DC: American Geophysical Union.

Kendall, J. M., & Silver, P. G. (1998). Investigating causes of D″ anisotropy. In M. Gurnis, M. E. Wysession, E. Knittle, & B. A. Buffett (Eds.), *The core-mantle boundary region, geodynamics series*, *Geophysical Monograph Series* (Vol. 28, pp. 97–118). Washington, DC: American Geophysical Union.

Kennett, B., Engdahl, E., & Buland, R. (1995). Constraints on seismic velocities in the Earth from travel-times. *Geophysical Journal International*, *122*(1), 108–124. https://doi.org/10.1111/j.1365-246X.1995.tb03540.x

Kito, T., Rost, S., Thomas, C., & Garnero, E. J. (2007). New insights into the *P*- and *S*-wave velocity structure of the D″ discontinuity beneath the Cocos plate. *Geophysical Journal International*, *169*(2), 631–645. https://doi.org/10.1111/j.1365-246X.2007.03350.x

Lay, T. (2015). 1.22 Deep Earth structure: Lower mantle and D. In G. Schubert (Ed.), *Treatise on geophysics* (2nd ed., pp. 683–723). Oxford: Elsevier.

Lay, T., & Garnero, E. J. (2004). Core–mantle boundary structures and processes. In R. S. J. Sparks & C. J. Hawkesworth (Eds.), *The state of the planet: Frontiers and challenges in geophysics*, *Geophysical Monograph Series* (Vol. 150, pp. 25–41). Washington, DC: American Geophysical Union.

Lay, T., & Garnero, E. J. (2007). Reconciling the post-perovskite phase with seismological observations of lowermost mantle structure. In K. Hirose, J. Brodholt, T. Lay, & D. Yuen (Eds.), *Post-perovskite, the last mantle phase transition*, *Geophysical Monograph Series* (Vol. 174, pp. 129–154). Washington, DC: American Geophysical Union.

Lay, T., Garnero, E. J., & Williams, Q. (2004). Partial melting in a thermo-chemical boundary layer at the base of the mantle. *Physics of the Earth and Planetary Interiors*, *146*(3-4), 441–467. https://doi.org/10.1016/j.pepi.2004.04.004

Long, M. D. (2009). Complex anisotropy in D″ beneath the eastern Pacific from SKS–SKKS splitting discrepancies. *Earth and Planetary Science Letters*, *283*(1-4), 181–189. https://doi.org/10.1016/j.epsl.2009.04.019

Long, M. D., & Lynner, C. (2015). Seismic anisotropy in the lowermost mantle near the Perm Anomaly. *Geophysical Research Letters*, *42*, 7073–7080. https://doi.org/10.1002/2015GL065506

Long, M. D., & Silver, P. G. (2009). Shear wave splitting and mantle anisotropy: Measurements, interpretations, and new directions. *Surveying in Geophysics*, *30*(4-5), 407–461. https://doi.org/10.1007/s10712-009-9075-1

Long, M. D., Xiao, X., Jiang, Z., Evans, B., & Karato, S. (2006). Lattice preferred orientation in deformed polycrystalline (Mg, Fe)O and implications for seismic anisotropy in D″. *Physics of the Earth and Planetary Interiors*, *156*(1–2), 75–88. https://doi.org/10.1016/j.pepi.2006.02.006

Lynner, C., & Long, M. D. (2012). Evaluating contributions to SK(K)S splitting from lower mantle anisotropy: a case study from station DBIC, Côte D'Ivoire. *Bulletin of Seismological Society of America*, *102*(3), 1030–1040. https://doi.org/10.1785/0120110255

Lynner, C., & Long, M. D. (2014a). Lowermost mantle anisotropy and deformation along the boundary of the African LLSVP. *Geophysical Research Letters*, *41*, 3447–3454. https://doi.org/10.1002/2014GL059875

Lynner, C., & Long, M. D. (2014b). Sub-slab anisotropy beneath the Sumatra and circum-Pacific subduction zones from source-side shear wave splitting observations. *Geochemistry, Geophysics, Geosystems*, *15*, 2262–2281. https://doi.org/10.1002/2014GC005239

Mainprice, D., Tommasi, A., Ferre, D., Carrez, P., & Cordier, P. (2008). Predicted glide systems and crystal preferred orientations of polycrystalline silicate Mg–perovskite at high pressure: Implications for the seismic anisotropy in the lower mantle. *Earth and Planetary Science Letters*, *271*(1-4), 135–144. https://doi.org/10.1016/j.epsl.2008.03.058

Mancinelli, N., Shearer, P., & Thomas, C. (2016). On the frequency dependence and spatial coherence of *PKP* precursor amplitudes. *Journal of Geophysical Research: Solid Earth*, *121*, 1873–1889. https://doi.org/10.1002/2015JB012768

Matzel, E., Sen, M. K., & Grand, S. P. (1996). Evidence for anisotropy in the deep mantle beneath Alaska. *Geophysical Research Letters*, *23*(18), 2417–2420. https://doi.org/10.1029/96GL02186

Maupin, V., Garnero, E. J., Lay, T., & Fouch, M. J. (2005). Azimuthal anisotropy in the D″ layer beneath the Caribbean. *Journal of Geophysical Research*, *110*, B08301. https://doi.org/10.1029/2004JB003506

Maupin, V., & Park, J. (2015). 1.09 Theory and observations—Wave propagation in anisotropic media. In G. Schubert (Ed.), *Treatise on geophysics* (2nd ed., pp. 277–305). Oxford: Elsevier.

Merkel, S., Kubo, A., & Miyagi, L. (2006). Plastic deformation of $MgGeO_3$ post-perovskite at lower mantle pressures. *Science*, *311*(5761), 644–646. https://doi.org/10.1126/science.1121808

Merkel, S., McNamara, A. K., & Kubo, A. (2007). Deformation of (Mg,Fe)SiO_3 post-perovskite and D″ anisotropy. *Science*, *316*(5832), 1729–1732. https://doi.org/10.1126/science.1140609

Miller, M. S., Allam, A. A., Becker, T. H. W., Di Leo, J. F., & Wookey, J. (2013). Constraints on the tectonic evolution of the westernmost Mediterranean and northwestern Africa from shear wave splitting analysis. *Earth and Planetary Science Letters*, *375*, 234–235. https://doi.org/10.1016/j.epsl.2013.05.036

Miyagi, L., Kanitpanyacharoen, W., Kaercher, P., Lee, K. K. M., & Wenk, H. R. (2010). Slip systems in $MgSiO_3$ post-perovskite: Implications for D″ anisotropy. *Science*, *329*(5999), 1639–1641. https://doi.org/10.1126/science.1192465

Montagner, J. P. (1998). Where can seismic anisotropy be detected in the Earth's mantle? In boundary layers.... *Pure and Applied Geophysics*, *151*(4), 223–256. https://doi.org/10.1007/s000240050113

Moore, M. M., Garnero, E. J., & Lay, T. (2002). D″ anisotropy beneath the Atlantic Ocean and the southern Pacific Ocean. *Eos Transactions American Geophysical Union*, *102*(B4), Fall Meeting Supplement, Abstract S12D-10), 8121–8135. https://doi.org/10.1029/96JB03830

Moore, M. M., Garnero, E. J., Lay, T., & Williams, Q. (2004). Shear wave splitting and waveform complexity for lowermost mantle structures with low-velocity lamellae and transverse isotropy. *Journal of Geophysical Research*, *109*, B02319. https://doi.org/10.1029/2003JB002546

Murakami, M., Hirose, K., Sata, N., Ohishi, Y., & Kawamura, K. (2004). Phase transition of $MgSiO_3$ perovskite in the deep lower mantle. *Science*, *304*(5672), 855–858. https://doi.org/10.1126/science.1095932

Nowacki, A. (2013). *Plate deformation from cradle to grave—Seismic anisotropy and deformation at mid-ocean ridges and in the lowermost mantle*, *Springer Theses* (Vol. 9). Berlin Heidelberg: Springer-Verlag Berlin Heidelberg. https://doi.org/10.1007/978-3-642-34842-6_2

Nowacki, A., Kendall, J. K., Wookey, J., & Pemberton, A. (2015). Mid-mantle anisotropy in subduction zones and deep water transport. *Geochemistry, Geophysics, Geosystems*, *16*, 764–784. https://doi.org/10.1002/2014GC005667

Nowacki, A., Walker, A. M., Wookey, J., & Kendall, J. M. (2013). Evaluating post-perovskite as a cause of D″ anisotropy in regions of palaeosubduction. *Geophysical Journal International*, *192*(3), 1085–1090. https://doi.org/10.1093/gji/ggs068

Nowacki, A., & Wookey, J. (2016). The limits of ray theory when measuring shear wave splitting in the lowermost mantle with *ScS* waves. *Geophysical Journal International*, *207*(3), 1573–1583. https://doi.org/10.1093/gji/ggw358

Nowacki, A., Wookey, J., & Kendall, J. M. (2010). Deformation of the lowermost mantle from seismic anisotropy. *Nature*, *467*(7319), 1091–1094. https://doi.org/10.1038/nature09507

Nowacki, A., Wookey, J., & Kendall, J. M. (2011). New advances in using seismic anisotropy, mineral physics and geodynamics to understand deformation in the lowermost mantle. *Journal of Geodynamics*, *52*(3-4), 205–228. https://doi.org/10.1016/j.jog.2011.04.003

Oganov, A. R., & Ono, S. (2004). Theoretical and experimental evidence for a postperovskite phase of MgSiO3 in Earth's D″ layer. *Nature*, *430*(6998), 445–448. https://doi.org/10.1038/nature02701

Panning, M. P., & Romanowicz, B. (2006). A three-dimensional radially anisotropic model of shear velocity in the whole mantle. *Geophysical Journal International*, *167*(1), 361–379. https://doi.org/10.1111/j.1365-246X.2006.03100.x

Polet, J., Silver, P., Beck, S., & Wallace, T. (2000). Shear wave anisotropy beneath the Andes from the BANJO, SEDA, and PISCO experiments. *Journal of Geophysical Research*, *105*(B3), 6287–6304. https://doi.org/10.1029/1999JB900326

Porritt, R. W., Becker, T. W., & Monsalve, G. (2014). Seismic anisotropy and slab dynamics from *SKS* splitting recorded in Colombia. *Geophysical Research Letters*, *41*, 8775–8783. https://doi.org/10.1002/2014GL061958

Pulliam, J., & Sen, M. (1998). Seismic anisotropy in the core-mantle transition zone. *Geophysical Journal International*, *135*(1), 113–128. https://doi.org/10.1046/j.1365-246X.1998.00612.x

Ritsema, J. (2000). Evidence for shear wave anisotropy in the lowermost mantle beneath the Indian Ocean. *Geophysical Research Letters*, *27*(7), 1041–1044. https://doi.org/10.1029/1999GL011037

Ritsema, J., Deuss, A., van Heijst, H. J., & Woodhouse, J. H. (2011). S40RTS: A degree-40 shear-velocity model for the mantle from new Rayleigh wave dispersion, teleseismic traveltime and normal-mode splitting function measurements. *Geophysical Journal International*, *184*(3), 1223–1236. https://doi.org/10.1111/j.1365-246X.2010.04884.x

Rokosky, J. M., Lay, T., & Garnero, E. J. (2006). Small-scale lateral variations in azimuthally anisotropic D″ structure beneath the Cocos Plate. *Earth and Planetary Science Letters*, *248*(1–2), 411–425. https://doi.org/10.1016/j.epsl.2006.06.005

Romanowicz, B., & Wenk, H. R. (2017). Anisotropy in the deep Earth. *Physics of the Earth and Planetary Interiors*, *269*, 58–90. https://doi.org/10.1016/j.pepi.2017.05.005

Rost, S., & Thomas, C. (2002). Array seismology: Methods and applications. *Reviews of Geophysics*, *40*(3), 1008. https://doi.org/10.1029/2000RG000100

Russell, S. A., Lay, T., & Garnero, E. J. (1998). Seismic evidence for small-scale dynamics in the lowermost mantle at the root of the Hawaiian hotspot. *Nature*, *396*(6708), 255–258. https://doi.org/10.1038/24364

Russell, S. A., Lay, T., & Garnero, E. J. (1999). Small-scale lateral shear velocity and anisotropy heterogeneity near the core-mantle boundary beneath the central Pacific imaged using broadband *ScS* waves. *Journal of Geophysical Research*, *104*(B6), 13,183–13,199. https://doi.org/10.1029/1999JB900114

Russo, R., & Silver, P. (1994). Trench-parallel flow beneath the Nazca plate from seismic anisotropy. *Science*, *263*(5150), 1105–1111. https://doi.org/10.1126/science.263.5150.1105

Saki, M., Thomas, C., Merkel, S., & Wookey, J. (2018). Detecting seismic anisotropy above the 410 km discontinuity using reflection coefficients of underside reflections. *Physics of the Earth and Planetary Interiors*, *274*, 170–183. https://doi.org/10.1016/j.pepi.2017.12.001

Scherbaum, F., Kruger, F., & Weber, M. (1997). Double beam imaging: Mapping lower mantle heterogeneities using combinations of source and receiver arrays. *Journal of Geophysical Research*, *102*(B1), 507–522. https://doi.org/10.1029/96JB03115

Schumacher, L., & Thomas, C. (2016). Detecting lower-mantle slabs beneath Asia and the Aleutians. *Geophysical Journal International*, *205*(3), 1512–1524. https://doi.org/10.1093/gji/ggw098

Schumacher, L., Thomas, C., & Abreu, R. (2018). Out-of-plane seismic reflections beneath the Pacific and their geophysical implications. *Journal of Geophysical Research: Solid Earth*, *123*, 2286–2302. https://doi.org/10.1002/2017JB014728

Schweitzer, J., Fyen, J., Mykkeltveit, S., & Kværna, T. P. (2012). Seismic arrays. In P. Bormann (Ed.), *New manual of seismological observatory practice (NMSOP-2)*, *IASPEI* (Chap. 9, pp. 1–52). Potsdam: Deutsches GeoForschungszentrum GFZ. http://doi.org/10.2312/GFZ.NMSOP-2

Sidorin, I., Gurnis, M., & Helmberger, D. (1999a). Dynamics of a phase change at the base of the mantle consistent with seismological observations. *Journal of Geophysical Research*, *104*(B7), 15,005–15,023. https://doi.org/10.1029/1999JB900065

Sidorin, I., Gurnis, M., & Helmberger, D. (1999b). Evidence for a ubiquitous seismic discontinuity at the base of the mantle. *Science*, *286*(5443), 1326–1331. https://doi.org/10.1126/science.286.5443.1326

Silver, P. G., & Chan, W. W. (1991). Shear-wave splitting and subcontinental mantle deformation. *Journal of Geophysical Research*, *96*(B10), 16,429–16,454. https://doi.org/10.1029/91JB00899

Silver, P. G., & Savage, M. K. (1994). The interpretation of shear-wave splitting parameters in the presence of 2 anisotropic layers. *Geophysical Journal International*, *119*(3), 949–963. https://doi.org/10.1111/j.1365-246X.1994.tb04027.x

Simmons, N. A., Forte, A. M., & Grand, S. P. (2009). Joint seismic, geodynamic and mineral physical constraints on three-dimensional mantle heterogeneity: Implications for the relative importance of thermal versus compositional heterogeneity. *Geophysical Journal International*, *177*(3), 1284–1304. https://doi.org/10.1111/j.1365-246X.2009.04133.x

Spieker, K., Wölbern, I., Thomas, C., Harnafi, M., & El Moudnib, L. (2014). Crustal and upper-mantle structure beneath the western Atlas Mountains in SW Morocco derived from receiver functions. *Geophysical Journal International*, *198*(3), 1474–1485. https://doi.org/10.1093/gji/ggu216

Stammler, K. (1993). Seismichandler—Programmable multichannel data handler for interactive and automatic processing of seismological analyses. *Computers and Geosciences*, *19*(2), 135–140. https://doi.org/10.1016/0098-3004(93)90110-Q

Teanby, N., Kendall, J. M., & Van der Baan, M. (2004). Automation of shear-wave splitting measurements using cluster analysis. *Bulletin of the Seismological Society of America*, *94*(2), 453–463. https://doi.org/10.1785/0120030123

Thomas, C., & Kendall, J. M. (2002). The lowermost mantle beneath northern Asia: (2) Evidence for D″ anisotropy. *Geophysical Journal International*, *151*(1), 296–308. https://doi.org/10.1046/j.1365-246X.2002.01760.x

Thomas, C., Kendall, J. M., & Lowman, J. (2004). Lower mantle seismic discontinuities and the thermal morphology of subducted slabs. *Earth and Planetary Science Letters*, *225*(1-2), 105–113. https://doi.org/10.1016/j.epsl.2004.05.038

Thomas, C., Kendall, J. M., & Weber, M. (2002). The lowermost mantle beneath northern Asia: (1) multi-azimuth studies of heterogeneity. *Geophysical Journal International*, *151*(1), 279–295. https://doi.org/10.1046/j.1365-246X.2002.01759.x

Thomas, C., & Weber, M. (1997). P-velocity heterogeneities in the lower mantle determined with the German Regional Seismic Network: Improvement of previous models and results of 2D modelling. *Physics of the Earth and Planetary Interrior*, *101*(1-2), 105–117. https://doi.org/10.1016/S0031-9201(96)03245-1

Thomas, C., Weber, M., Wicks, C. W., & Scherbaum, F. (1999). Small scatterers in the lower mantle observed at German broadband arrays. *Journal of Geophysical Research*, *104*(B7), 15,073–15,088. https://doi.org/10.1029/1999JB900128

Thomas, C., Wookey, J., Brodholt, J., & Fieseler, T. (2011). Anisotropy as cause for polarity reversals of D″ reflections. *Earth and Planetary Science Letters*, *307*(3-4), 369–376. https://doi.org/10.1016/j.epsl.2011.05.011

Tommasi, A., Goryaeva, A., Carrez, P., Cordier, P., & Mainprice, D. (2018). Deformation, crystal preferred orientations, and seismic anisotropy in the Earth's D″ layer. *Earth and Planetary Science Letters*, *492*, 35–46. https://doi.org/10.1016/j.epsl.2018.03.032

van der Hilst, R. D., de Hoop, M. V., Wang, P., Shim, S. H., Ma, P., & Tenorio, L. (2007). Seismostratigraphy and thermal structure of Earth's core–mantle boundary region. *Science*, *315*(5820), 1813–1817. https://doi.org/10.1126/science.1137867

van der Hilst, R. D., Widiyantoro, S., & Engdahl, E. R. (1997). Evidence for deep mantle circulation from global tomography. *Nature*, *386*(6625), 578–584. https://doi.org/10.1038/386578a0

van der Meer, D. G., Spakman, W., van Hinsbergen, D. J. J., Amaru, M. L., & Torsvik, T. H. (2010). Towards absolute plate motions constrained by lower-mantle slab remnants. *Nature Geoscience*, *3*(1), 36–40. https://doi.org/10.1038/ngeo708

van der Meer, D. G., van Hinsbergen, D. J. J., & Spakman, W. (2018). Atlas of the underworld: Slab remnants in the mantle, their sinking history, and a new outlook on lower mantle viscosity. *Tectonophysics*, *723*, 309–448. https://doi.org/10.1016/j.tecto.2017.10.004

Vidale, J. E., & Hedlin, M. A. H. (1998). Evidence for partial melt at the core mantle boundary north of Tonga from the strong scattering of seismic waves. *Nature*, *391*(6668), 682–685. https://doi.org/10.1038/35601

Walker, A. M., Forte, A. M., Wookey, J., Nowacki, A., & Kendall, J. M. (2011). Elastic anisotropy of D″ predicted from global models of mantle flow. *Geochemistry, Geophysics, Geosystems*, *12*, Q10006. https://doi.org/10.1029/2011GC003732

Walker, A. M., & Wookey, J. (2012). MSAT—A new toolkit for the analysis of elastic and seismic anisotropy. *Computers and Geosciences*, *49*, 81–90. https://doi.org/10.1016/j.cageo.2012.05.031

Wallace, M., & Thomas, C. (2005). Investigating D″ structure beneath the North Atlantic. *Physics of the Earth and Planetary Interiors*, *151*(1-2), 115–127. https://doi.org/10.1016/j.pepi.2005.02.001

Walpole, J., Wookey, J., Kendall, J. M., & Masters, T. (2017). Seismic anisotropy and mantle flow below subducting slabs. *Earth and Planetary Science Letters*, *465*, 155–167. https://doi.org/10.1016/j.epsl.2017.02.023

Walte, N. P., Heidelbach, F., Miyajima, N., Frost, D. J., Rubie, D. C., & Dobson, D. P. (2009). Transformation textures in post-perovskite: Understanding mantle flow in the D″ layer of the Earth. *Geophysical Research Letters*, *36*, L04302. https://doi.org/10.1029/2008GL036840

Wang, Y., & Wen, L. (2007). Complex seismic anisotropy at the border of a very low velocity province at the base of the Earth's mantle. *Journal of Geophysical Research*, *112*, B09305. https://doi.org/10.1029/2006JB004719

Weber, M. (1993). *P*- and *S*-wave reflections from anomalies in the lowermost mantle. *Geophysical Journal International*, *115*(1), 183–210. https://doi.org/10.1111/j.1365-246X.1993.tb05598.x

Weber, M., & Davis, J. P. (1990). Evidence of a laterally variable lower mantle structure from *P*- and *S*-waves. *Geophysical Journal International*, *102*(1), 231–255. https://doi.org/10.1111/j.1365-246X.1990.tb00544.x

Weber, M., & Körnig, M. (1990). Lower mantle inhomogeneities inferred from *PcP* precursors. *Geophysical Research Letters*, *17*(11), 1993–1996. https://doi.org/10.1029/GL017i011p01993

Weber, M., & Körnig, M. (1992). A search for anomalies in the lowermost mantle using seismic bulletins. *Physics of the Earth and Planetary Interiors*, *73*(1-2), 1–28. https://doi.org/10.1016/0031-9201(92)90104-4

Wessel, P., & Smith, W. H. F. (1995). New version of the Generic Mapping Tools. *Eos, Transactions American Geophysical Union*, *76*(33), 329–329. https://doi.org/10.1029/95EO00198

Wolfe, C., & Silver, P. (1998). Seismic anisotropy of oceanic upper mantle: Shear wave splitting methodologies and observations. *Journal of Geophysical Research*, *103*(B1), 749–771. https://doi.org/10.1029/97JB02023

Wookey, J., & Kendall, J. M. (2007). Seismic anisotropy of post-perovskite and the lowermost mantle. In K. Hirose, J. Brodholt, T. Lay, & D. Yuen (Eds.), *Post-perovskite, the last mantle phase transition*, *Geophysical Monograph Series* (Vol. 174, pp. 171–189). Washington, DC: American Geophysical Union.

Wookey, J., & Kendall, J. M. (2008). Constraints on lowermost mantle mineralogy and fabric beneath Siberia from seismic anisotropy. *Earth and Planetary Science Letters*, *275*(1-2), 32–42. https://doi.org/10.1016/j.epsl.2008.07.049

Wookey, J., Kendall, J. M., & Rümpker, G. (2005). Lowermost mantle anisotropy beneath the north Pacific from differential *S-ScS* splitting. *Geophysical Journal International*, *161*(3), 829–838. https://doi.org/10.1111/j.1365-246X.2005.02623.x

Wookey, J., Stackhouse, S., Kendall, J. M., Brodholt, J. P., & Price, G. D. (2005). Efficacy of the post-perovskite phase as an explanation of lowermost mantle seismic properties. *Nature*, *438*(7070), 1004–1007. https://doi.org/10.1038/nature04345

Wuestefeld, A., Al-Harrasi, O., Verdon, J. P., Wookey, J., & Kendall, J. M. (2010). A strategy for automated analysis of passive microseismic data to image seismic anisotropy and fracture characteristics. *Geophysical Prospecting*, *58*(5), 755–773. https://doi.org/10.1111/j.1365-2478.2010.00891.x

Wysession, M. E., Lay, T., Revenaugh, J., Williams, Q., Garnero, E. J., Jeanloz, R., & Kellogg, L. (1998). The D″ discontinuity and its implications. In M. Gurnis, M. E. Wysession, E. Knittle, & B. A. Buffett (Eds.), *The core–mantle boundary region*, *Geophysical Monograph Series* (Vol. 28, pp. 273–298). Washington, DC: American Geophysical Union.

Yamazaki, D., & Karato, S. I. (2007). Lattice-preferred orientation of lower mantle materials and seismic anisotropy in the D″ layer. In K. Hirose, J. Brodholt, T. Lay, & D. Yuen (Eds.), *Post-perovskite, the last mantle phase transition*, *Geophysical Monograph Series* (Vol. 174, pp. 69–78). Washington, DC: American Geophysical Union. https://doi.org/10.1029/174GM07

Yamazaki, D., Yoshino, T., Ohfuji, H., Ando, J. I., & Yoneda, A. (2006). Origin of seismic anisotropy in the D″ layer inferred from shear deformation experiments on postperovskite phase. *Earth and Planetary Science Letters*, *252*(3-4), 372–378. https://doi.org/10.1016/j.epsl.2006.10.004

Yao, Y., Whittaker, S., & Thorne, M. S. (2015). D″ discontinuity structure beneath the North Atlantic from *Scd* observations. *Geophysical Research Letters*, *42*, 3793–3801. https://doi.org/10.1002/2015GL063989

Zhao, D. (2004). Global tomographic images of mantle plumes and subducting slabs: Insight into deep Earth dynamics. *Physics of the Earth and Planetary Interiors*, *146*(1-2), 3–34. https://doi.org/10.1016/j.pepi.2003.07.032